Bioactive Materials 59 (2026) 288–304

Contents lists available at ScienceDirect

Bioactive Materials

journal homepage: www.keaipublishing.com/en/journals/bioactive-materials

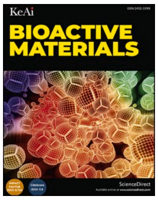

A large puncture closer of aortic wall by multi-memory actions with thrombo-hemodynamic control

Sungwoo Cho [a,b,1], Hyun-Su Ha [c,1], Sangmin Lee [a,1], Hyunjae Kim [a], Seok Joon Lee [a], Jueun Kim [a,e], Yerin Lee [a], Kang Suk Lee [a], Hyun-Chel Joo [d,*], Hak-Joon Sung [a,e,**]

[a] Department of Medical Engineering, Yonsei University College of Medicine, 50-1 Yonsei-ro, Seodaemun-gu, Seoul, 03722, Republic of Korea
[b] Department of Biomedical Science, Yonsei University College of Medicine, 50-1 Yonsei-ro, Seodaemun-gu, Seoul, 03722, Republic of Korea
[c] Division of Cardiology Department of Internal Medicine, Severance Cardiovascular Hospital, Yonsei University College of Medicine, 50-1 Yonsei-ro, Seodaemun-gu, Seoul, 03722, Republic of Korea
[d] Division of Cardiovascular Surgery, Department of Thoracic and Cardiovascular Surgery, Severance Cardiovascular Hospital, Yonsei University College of Medicine, 50-1 Yonsei-ro, Seodaemun-gu, Seoul, 03722, Republic of Korea
[e] Department of Brain Korea 21 FOUR Project for Medical Science, Yonsei University College of Medicine, 50-1 Yonsei-ro, Seodaemun-gu, Seoul, 03722, Republic of Korea

ARTICLE INFO

Keywords:
Shape memory polymer
Vascular closure device
Hemostasis
Platelet aggregation
Shape recovery force

ABSTRACT

The vascular wall regulates the pattern and pressure of blood flow. In cardiovascular interventions, catheters are deployed by puncturing the vessel wall, without exception. Despite continuous progress, the outcomes remain highly operator-dependent, and large punctures with high-pressure bleeding continue to pose clinical challenges. As a translatable solution, this study introduces a shape memory vascular wall plug (VWP) that automates both the Body and Wing functions within a single component, supported by a Ring assembly to maximize pressure resistance. The VWP is deployed into a 6-mm puncture in a porcine thoracic aorta under peak blood pressure, and shape recovery is triggered by a 45°C saline flush to enable automated activation. Upon recovery, Body expansion combined with Ring compression tightly seals the puncture tract. The curved Wing induces hemostatic sealing and then flattens to maintain healthy blood flow and physiologic pressures. The VWP achieves suturing-level performance in aortic puncture closure, demonstrating effective hemostasis, patency, and endothelialization. The flow-blockage ratio required to balance hemostasis with hemodynamics is computationally modeled and validated using whole-blood microfluidics. Pressure resistance is maximized by tuning Ring strain through polymer blending, indicating multi-level strategies in polymer, device design, and memory function to advance the vascular closure technology.

1. Introduction

Most interventional treatments for cardiovascular disorders require catheter deployment, which inevitably leaves a puncture in the vascular wall upon removal [1,2]. Because the vascular wall governs the pattern and pressure of blood flow, improper management of puncture closure can lead to severe bleeding and downstream clinical complications throughout the circulatory system [3–5]. Traditional approaches include manual compression, suturing, clipping, or the use of collagen-based plugs [6,7]. Compared with these methods, advances in vascular closure devices (VCD) have aimed to improve ease of use, accelerate hemostasis, and reduce costs while ensuring tight and reliable closure of access sites [8,9]. Continued progress in VCD technology has substantially reduced complications such as incomplete hemostasis, device malfunctions, recurrent bleeding, and pseudoaneurysm formation [6,10]. However, these complications often become “spilled water”,

---

Peer review under the responsibility of editorial board of Bioactive Materials.

* Corresponding author. Division of Cardiovascular Surgery, Department of Thoracic and Cardiovascular Surgery, Severance Cardiovascular Hospital, Yonsei University College of Medicine, 50-1 Yonsei-ro, Seodaemun-gu, Seoul 03722, Republic of Korea.

** Corresponding author. Department of Medical Engineering, Yonsei University College of Medicine, 50-1 Yonsei-ro, Seodaemun-gu, Seoul, 03722, Republic of Korea.

E-mail addresses: vietcomm@yuhs.ac (H.-C. Joo), hj72sung@yuhs.ac (H.-J. Sung).

[1] These authors contributed equally to this work.

https://doi.org/10.1016/j.bioactmat.2025.12.042
Received 22 August 2025; Received in revised form 28 November 2025; Accepted 22 December 2025
Available online 30 December 2025
2452-199X/© 2025 The Authors. Publishing services by Elsevier B.V. on behalf of KeAi Communications Co. Ltd. This is an open access article under the CC BY-NC-ND license (http://creativecommons.org/licenses/by-nc-nd/4.0/).

requiring additional interventions and prolonged hospital stays, ultimately increasing patient morbidity and healthcare costs [8,11].

A persistent unmet need in current VCD practice is that failure in the initial positioning of a device often makes reattempting closure difficult or even infeasible [12,13]. Furthermore, the handling of multiple deployment tools is technically demanding, particularly for trainees, necessitating specialized training and clinical experience to ensure proficiency [12,14,15]. Achieving easy, adjustable plugging with automated deployment represents a promising direction to advance the technology. Another unmet clinical need is the lack of large-sized devices capable of closing substantial punctures around 6 mm (e.g., 18 Fr) in diameter [16,17]. As puncture size increases, bleeding pressure also rises, making vascular wall closure more challenging. Addressing this issue requires enhanced sealing efficiency akin to platelet aggregation to counteract high-pressure bleeding while supporting the body's innate hemostatic responses. Additionally, maintaining healthy blood flow and physiological pressure through the promotion of laminar flow is necessary to prevent stenosis, while endothelialization and the suppression of vascular remodeling remain key considerations [18]. Collectively, the new paradigm of VCD development should adopt adjustable and automatic deployment to close large punctures while simultaneously controlling hemostatic and hemodynamic conditions in addition to vascular wall remodeling.

As a foundational strategy, the use of shape memory polymers (SMPs) enables automatic device deployment by triggering structural recovery with warm water as a heat source [19–21]. Because the structure can be temporarily fixed to support initial positioning prior to heating, the plugging site can be repeatedly adjusted, after which the remaining deployment occurs automatically once warmed, independent of user skill. Memory programming can be applied to multiple components of the device, allowing user-specified directional recovery of each part. This advantage enables tight plugging like bolt-and-nut assembly, while also allowing controlled modulation of blood flow from temporary blockage to patency. Owing to the versatility and adaptability of SMPs [22–27], the recovery forces driving Body expansion, Ring squeezing, and Wing spreading can be tuned by adjusting strain levels, polymer blending, and phase separation.

When an injury generates punctures in blood vessels, the body's innate defense mechanism induces thrombosis to stop bleeding regardless of the puncture size, ultimately reaching hemostasis [28,29]. Platelets play a central role in this process. They are recruited to the injury site through interactions between platelets GPIb and von Willebrand factor (vWF) exposed on damaged endothelial cells (ECs) [30]. Fibrinogen then activates the platelets, enabling formation of a thrombotic plug that seals the wound, demonstrating that hemostasis is inherently capable of sealing even large punctures. This mechanism can be purposely leveraged during VCD deployment: partial flow blockage that causes platelets to bump against the obstructing surface, after which the resulting shear gradient further enhances platelet activation and aggregation [31,32]. Clinically, this is analogous to stenotic lesions, where partial obstruction and altered shear gradients promote platelet responses [33,34].

As an unprecedented VCD concept, this study presents a memory programmable vascular wall plug (VWP) featuring a Body and Ring integrated into a single component, with subsequent Ring assembly, designed around the following principles. i) The initial deployment step allows easy and repeatable adjustments prior to triggering shape recovery. ii) Shape recovery automates the deployment process regardless of operator skill. iii) Directional shape recovery should enable Body expansion with Ring squeezing for tight puncture plugging. iv) A curved Wing should partially block blood flow to recruit platelets through bumping, with subsequent shear-induced activation. v) The resulting hemostatic sealing should enhance the overall plugging efficiency. vi) Burst-pressure resistance should be maximized by controlling Ring strain and SMP blending to optimize phase behavior. The flow-blockage ratio required to regulate hemostasis under varying hemodynamic conditions is characterized using computational fluid dynamics (CFD). A microfluidic vessel model with VWP deployment further confirms the CFD findings under mouse whole blood flow. The VWP effectively seals a large-bore (6 mm) puncture in the porcine thoracic aorta under maximal physiological blood pressure. In terms of hemostasis, endothelialization, and preservation of healthy vascular wall histology, the rapid performance of the VWP is comparable to conventional suturing despite the latter's longer procedural time.

2. Materials and methods

2.1. Synthesis of shape memory polymer (SMP)

SMP was synthesized via ring-opening polymerization (P: poly) of caprolactone (CL) and glycidyl methacrylate (GMA) monomers and supplied by TMD LAB Co., Ltd [22]. Briefly, CL (315 mmol) and dipentaerythritol (0.5 mmol) were reacted at 110°C for 10 min in a three-neck round-bottom flask, followed by the addition of hydroquinone (3.5 mmol, 1:10 M ratio to GMA) as an auto-crosslinking inhibitor. GMA (35 mmol) was then added to the mixture with stirring for an additional 10 min. Next, 1,5,7-triazabicyclo[4.4.0]dec-5-ene (TBD, 1 mmol) dissolved in acetonitrile (4 mL) was added to the reaction mixture, which was maintained at 110°C for 6 h under a nitrogen atmosphere. The reaction mixture was cooled to room temperature (25°C) and dissolved in chloroform (30 mL). The solution was precipitated in cold diethyl ether (800 mL, 4°C), yielding a white solid. The final SMP product was vacuum dried (OV4-30, Jeio Tech) at room temperature and defined as 6-arm x% PCL-co-y% PGMA (x, y%: molar ratio). All chemicals were purchased from Sigma Aldrich.

2.2. Characterization of 6-arm SMP (x% PCL-co-y% PGMA) and PCL blends

Test film preparation: Solutions were prepared by dissolving in N-methyl-2-pyrrolidone (NMP, St. Louis, MO, Sigma Aldrich). Films were prepared by dissolving each blend (1 g) of SMP with PCL ($M_n = 80,000$ Da, Sigma Aldrich) at varying SMP/PCL weight ratios in 1 mL NMP. 2-hydroxy-4'-(2-hydroxyethoxy)-2-methylpropiophenone (5 mg, Irgacure 2959, Sigma Aldrich) was added as a photoinitiator. The mixture was stirred at 60°C for 2 h, cast onto a transparent glass substrate, and covered with another glass slide in a sandwich format. For crosslinking, the assembly was exposed to UV irradiation (365 nm, 265 mJ cm^{-1}) for 200 s. The film was removed, washed with distilled water to eliminate residual solvent, and vacuum-dried at room temperature for 24 h.

Structure, composition, and surface: ^{1}H NMR spectroscopy was performed using a single z-axis gradient inverse probe at 400 MHz. Fourier transform infrared (FTIR) analyses were carried out using a Nicolet Summit FTIR spectrometer (Thermo Fisher Scientific) by obtaining FTIR spectra at room temperature with a resolution of 2 cm^{-1} with 64 scans per sample. Surface morphology was imaged by Field-emission Scanning Electron Microscopy (FE-SEM, JEOL Ltd.) after sputter-coating with a thin platinum layer, using an accelerating the voltage of 15 kV.

Atomic force microscopy (AFM): SMP/PCL films (thickness: 500 μm) were heated to 60°C and cooled at room temperature for 24 h, followed by incubation in liquid nitrogen. Crystalline surfaces were imaged by AFM (NX-10, Park Systems Corp., Gyeonggi-do, Republic of Korea). A position-controllable probe (Standard Contact Mode AFM Probe, Probes, Seoul, Republic of Korea) was scanned in a raster pattern to generate 3D surface maps. Multiple imaging repetitions were performed to obtain average roughness for statistical analysis.

Thermal properties: Films were characterized using a differential scanning calorimetry (DSC, Discovery DSC25, TA Instruments) and a laser flash apparatus (LFA, LFA 467, NETZSCH). Heat flow (q), crystallization temperature (T_c), crystallization enthalpy (ΔH_c), melting temperature (T_m), melting enthalpy (ΔH_m) and specific heat capacity

(C_p) were determined from DSC thermograms. DSC was operated in Tzero pans (T191218, T191023, TA Instruments) following the temperature program: Samples were (i) heated to 150°C at a rate of 10°C min^{-1}, equilibrated for 5 min; (ii) cooled to −80°C at a rate of 10°C min^{-1}, equilibrated for 5 min; and iii) heated to 150°C at a rate of 10°C min^{-1}. After coating SMP/PCL blend films with graphite, thermal diffusivity (α) was measured using the LFA 467 at 25°C and 37°C. Degree of crystallinity (χ_c), specific heat capacity, and thermal conductivity (λ) were calculated using Equations (1)–(3), respectively.

$$\text{Degree of crystallinity } \chi_c(\%) = \frac{\Delta H_c}{\Delta H_c^{\circ}} \times 100\%, \text{ where } \Delta H_c^{\circ}\ \left(139.5\ \text{J g}^{-1}\right) \text{ is the enthalpy of 100\% crystalline PCL.} \tag{1}$$

$$\text{Specific heat capacity } C_p(\%) = \frac{q}{\beta} \times 100, \tag{2}$$

$$\text{Thermal conductivity } \lambda = \alpha \times \rho \times C_p, \text{ where } \rho \text{ is the density of each sample.} \tag{3}$$

Mechanical properties: Films were characterized using a dynamic mechanical analyzer (DMA, Discovery DMA850, TA Instruments) to determine toughness, elastic modulus, and shape recovery force from stress–strain curves. Film samples [5 mm (length) × 5 mm (width) × 0.2 mm (thickness)] and cylindrical samples [8 mm (diameter) × 1.5 mm (thickness)] were used for tensile and compression tests, respectively. The Young's modulus and shape recovery force were measured in strain-controlled mode under 2 % min^{-1} using DMA following this stress-controlled protocol: Samples were (i) heated to 60°C at a rate of 4°C min^{-1} under consistent strains, equilibrated for 10 min; (ii) stretched to the target strain at a rate of 4 % min^{-1} (tensile test) or compressed at 1 % min^{-1} (compression test); (iii) cooled to −10°C under constant strain, equilibrated for 5 min; (iv) reheated to 60°C at a rate of 4°C min^{-1} under consistent strain conditions, and equilibrated for 5 min. The Young's modulus was calculated from the slope of the stress-strain curve in the initial linear region (strain less than 10 %). Shape recovery force was examined during step (iv) using SMP/PCL blend films [5 mm (length) × 5 mm (width) × 0.2 mm (thickness)] stretched to 50, 100, or 150 %. When the loading weight increased, the maximum weight and pull-up degree were determined after heating to trigger shape recovery.

Thermomechanical analysis for shape memory 5 cycles: Thermomechanical analysis of three compositions (SMP/PCL: 100/0, 95/5, and 90/10) was carried out using DMA under controlled cyclic stress for five consecutive cycles (N): i) Films were heated to 60°C and equilibrated for 10 min (original permanent shape, ε_p (0)), then a tensile stress of 50 kPa was applied at 4 kPa min^{-1} to program a temporary shape. ii) The films were cooled to −10°C at a rate of 2°C min^{-1} and equilibrated for 10 min to fix the shape (maximum strain, ε_1 (N)). iii) Tensile load was removed at 5 kPa min^{-1} to yield the temporary shape (ε_t (N)). iv) Samples were reheated to 60°C at 2°C min^{-1} to restore the original shape (ε_p (N)). Shape memory efficiency in each cycle (N) was quantified using the shape recovery ratio (R_r) and shape fixity ratio (R_f). R_r represents the ability of the SMP to recover its original shape after mechanical deformation [Equation (4)], and R_f represents the ability to retain the temporary shape after tensile load removal [Equation (5)].

$$R_r(N)(\%) = \frac{\varepsilon_1(N) - \varepsilon_p(N)}{\varepsilon_1(N) - \varepsilon_p(N-1)} \times 100\% \tag{4}$$

$$R_f(N)(\%) = \frac{\varepsilon_t(N)}{\varepsilon_1(N)} \times 100\% \tag{5}$$

Viscoelastic properties: Rectangular specimens [5 mm (length) × 5 mm (width) × 0.2 mm (thickness)] were mounted in film clamps and subjected to frequency sweep tests using DMA in controlled stress mode. The test specimens were subjected to a constant stress amplitude of 0.1 MPa with systemic variation of frequencies from 0 to 100 Hz at 37°C. The frequency sweep was performed within the linear viscoelastic region to obtain the results of intrinsic material properties without structural alteration. Fatigue testing evaluated the stability and durability of VWP under continuous cyclic loading analogous arterial contraction. The test program of frequency sweep was modified to require high-cycle fatigue by subjecting specimens to 7 × 10^7 cycles at 60 Hz at 37°C under 0.1 MPa stress. The 60 Hz frequency was applied because the plateau region of storage modulus (E′) was shown in the frequency sweep test (0–100 Hz), ensuring linear viscoelastic behavior during fatigue analysis.

Sterilization of SMP/PCL blends: SMP/PCL samples (100/0, 95/5, and 90/10) were sterilized using ethylene oxide (EO) gas. Chemical structures before and after sterilization were analyzed using ^{1}H NMR by dissolving samples in chloroform-d (Sigma Aldrich). Cytotoxicity was assessed by culturing L929 murine fibroblasts and the Cell Counting Kit-8 (CCK-8) assay (Promega, Madison, WI, USA) according to the manufacturer's instructions. Test samples were incubated in culture medium for 72 h to collect extracts, which were applied to L929 cells (5 × 10^3 cells/mL) cultured in 96-well microplates for 24 h. CCK-8 solution was added and incubated for 2 h at 37°C. Absorbance of each sample was measured at 450 nm using a microplate reader (SpectraMax 340; Molecular Devices, Sunnyvale, CA, USA) and normalized to the values prior to EO sterilization (100 %).

Long-term stability upon accelerated degradation: Long-term stability was evaluated using accelerated degradation of SMP, following American Society for Testing and Materials (ASTM) F1980 standard. Arrhenius equations [6–8] were applied to calculate accelerated aging time (AAT), aging factor (AAF), and accelerated aging temperature (T_{AA}) for a given real-time duration (desired time: DT).

$$\text{AAT} = \frac{DT}{AAF} \tag{6}$$

$$\text{AAF} = Q_{10}^{\left(\frac{T_{AA}-T_{AT}}{10}\right)} \tag{7}$$

$$Q_{10} = 2.0 \tag{8}$$

Ambient temperature (T_{AT}) was set to 37°C to reflect physiological conditions, and $Q_{10=}2.0$ was used as the industry standard value. Using equations [6–8], the weight loss (%) upon accelerated degradation at 70 ± 2°C for 37, 74, or 111 days was equivalent to DT for 1, 2, or 3-years of real-time degradation. SMP tubes (diameter: 6 mm, thickness: 500 μm) were incubated in phosphate buffer saline (PBS, pH 7.4) at 70 ± 2°C with weight measurements at day 0 (initial), 37, 74, and 111 (final), followed by calculating the weight loss (%) from the initial mass at each time point.

2.3. VWP production and characterization

Fabrication: Master molds of VWP parts were designed using Autodesk Fusion 360 software (Autodesk), and the mold structures were 3D printed (Photon Mono M5s, Anycubic) using polydimethylsiloxane

(PDMS, SYLGARD 184, Dow Corning) mixed with curing agent (10:1 wt/wt). Each SMP/PCL solution was cast into the PDMS molds and crosslinked under UV irradiation (365 nm, 265 mJ cm^{-1}) for 200 s using UV Crosslinker (CL-3000L, Analytik Jena). The products were washed with distilled water to remove residual solvent and vacuum-dried at room temperature for 24 h.

Shape programming: For shape programming, samples were placed on a stainless-steel dish and (i) heated to 60°C for 10 min, (ii) deformed to a temporary shape, (iii) cooled to −10°C under constant strain for 5 min (shape fixing), and (vi) returned to room temperature. As temporary shapes, film samples were stretched by 100 %; Body was compressed by 25 % to reach a 6 mm diameter using a crimping tool (HSC8 16-6, CLAMPLUS); and Wing was folded at 90° in a PDMS mold. Ring was stretched by 50, 100, or 150 % to enlarge the diameter to 9, 12, and 15 mm, respectively, using a customized stretcher designed in Fusion 360 software (Autodesk).

Triggering conditions for shape recovery First, film samples [5 mm (width) × 15 mm (length)] were programmed to determine the recovery time using the test compositions (SMP/PCL: 100/0, 95/5 and 90/10) after shape programming at 100 % stretching (temporary shape) as described above. Each film was then heated up to test recovery temperature (39°C, 42°C, or 45°C), selected to allow efficient shape recovery without tissue damage. Shape recovery was triggered by syringe flow at 2.0 mL s^{-1} matching the same heating means in the in vitro phantom, ex vivo carotid, and in vivo experiments. Recovery time was defined as the time required to return to the original shape and was measured in triplicate (N = 3).

VWP fixity and recovery ratio for 5 programming cycles: To assess reproducibility, the three parts (Ring, Body, and Wing) of VWP underwent 5 shape programming cycles to exam maintenance of shape fixity and recovery ratios. The temporary shapes were produced on stainless-steel dishes following the same programming as described above. The shape recovery of each part was triggered by applying 45°C water flow from a syringe at 2.0 mL s^{-1}, the same heating means in the in vitro phantom, ex vivo carotid, and in vivo experiments. The syringe flow was applied for 15 s because the SMP/PCL(95/5) films underwent shape recovery within the time frame upon variation of the trigger temperature (39°C, 42°C, or 45°C). The angle (Wing) and diameter (Body and Ring) were measured using ImageJ software (Fiji) after imaging the original, temporary, and recovered shapes across the 5 cycles. Shape fixity and recovery ratios were calculated based on the degree of shape matching as the cycle increased, with three samples used to ensure the batch-to-batch reproducibility (N = 3).

2.4. VWP delivery and deployment in a phantom model of thoracic aorta

A silicone tube [inner diameter (ID): 8 mm, outer diameter (OD): 10 mm, Korea Ace Scientific] was used as a thoracic aorta phantom. A 6 mm puncture was generated using a biopsy punch (Acu-Punch, Acuderm). Temporary shapes of the three VWP parts were prepared. Body was penetrated with 4-0 vicryl thread to stabilize positioning through the puncture. Body was mounted at the catheter tip (ID: 6 mm, OD: 7 mm) to facilitate Wing deployment. Ring was placed outside the catheter for tagging onto Body using a pusher. As a clinic-mimetic procedure, i) a sheath was positioned over the puncture; ii) the catheter was advanced through the sheath to place Body and Wing into the puncture; iii) Ring was pushed through the gap between the sheath and catheter using pusher 2; iv) Body and Wing were pushed into the puncture using pusher 1 while the stabilizing thread was removed so that Body and Wing were stably positioned to be ready for plugging; v) the catheter and pusher were removed, and vi) 45°C saline was infused through the sheath using a syringe at 2.0 mL s^{-1} for 15 s to trigger shape recovery of all three VWP parts. Leakage disappearance confirmed successful plugging.

2.5. Burst pressure analysis

In vitro: A silicone tube (inner diameter: 8 mm, outer diameter: 10 mm, KoreaAceScientific) was used as a phantom model of the thoracic aorta, and the tube wall was punctured using a 6 mm biopsy punch (Acu-Punch, Acuderm). After sealing the tube outlet to prevent leakage, a stopcock was used to connect the tube inlet, syringe, and pressure measurement system with the pressure transmitter (PNS, Nuritech) and digital indicator (PD1, Nuritech). VWP Rings (inner diameter: 6 mm) were stretched to 50 %, 100 %, and 150 % strains as deployable temporary shapes. The Body/Wing part of VWP was positioned in the puncture and each test ring was deployed, followed by warm saline treatment to induce self-locking via shape recovery. Distilled water was injected into the tube inlet using a syringe pump (Standard PHD ULTRA CP, Harvard Apparatus) until leakage occurred while monitoring the flow pressure.

Ex vivo: After euthanizing the pig, carotid arteries (inner diameter: 3.5 mm, outer diameter: 5.5 mm) were harvested in accordance with the Institutional Animal Care and Use Committee of Yonsei University College of Medicine (IACUC, approval number: 2024-0296). A 3 mm puncture was created on the artery wall using biopsy punch (Acu-Punch, Acuderm). Rings (inner diameter: 3 mm) were stretched to strains of 0 % and 100 % and deployed into the puncture, and burst pressure was measured following the same method as the in vitro test.

2.6. Computational fluid dynamics (CFD)

CFD simulations were performed to analyze shear and flow velocity changes by varying the flow blockage ratio using Fluent in ANSYS software (ANSYS 2020 R1). The thoracic aorta model was simplified to a tube [30 mm (width) x 1.0 mm (length) x 0.02 mm (height)] with 0.2 and 0.8 mm void areas for VWP deployment. The mesh was generated with 253,343 to 253,456 elements with sizes between 1×10^{-6} m and 2×10^{-5} m. Blood density and viscosity under laminar flow were set to 1060 kg m^{-3} and 0.0032 kg m^{-1} s^{-1}, respectively. The shear rate ($\dot{\gamma}$) was calculated by summing the absolute values of y-directional velocity gradients of the velocity components (u, v, w) as formulated in Equation (4):

$$\dot{\gamma} = \sqrt{\left(\frac{\partial u}{\partial y}\right)^2} + \sqrt{\left(\frac{\partial v}{\partial y}\right)^2} + \sqrt{\left(\frac{\partial w}{\partial y}\right)^2} \tag{9}$$

The input velocity was varied from 6 to 30 mm s^{-1}.

A model of puncture closure by VWP in porcine thoracic aorta was simulated using CFD by varying hemodynamic conditions. This model geometry [100 mm (width) × 6.0 mm (length) × 6.0 mm (height)] included void areas of 0.2 and 1.2 mm for VWP deployment. The finite volume mesh was generated using 20,262 to 21,547 elements with sizes ranging from 9.7×10^{-5} to 2.5×10^{-3} m. Blood density and viscosity under laminar flow were set to 1060 kg m^{-3} and 0.0032 kg m^{-1} s^{-1}, respectively.

2.7. Blood microfluidic model

Blood collection: Mouse whole blood was collected in accordance with the IACUC (approval number: 2022-0050). C57BL/6 mice (6 weeks old, male, Orient Bio) were anesthetized with Zoletil (50 mg kg^{-1}, Virbac Korea) and xylazine (10 mg kg^{-1}, Rompun, Bayer Korea) by intramuscular injection. The heart was exposed and punctured, and blood was collected in sodium citrate tubes (3.2 % (vol/vol), 2 mL, Greiner Bio-One).

Chip fabrication: A microfluidic chip was designed to deploy the miniature VWP Wing (mVWP) under circulating mouse whole blood. PDMS molds were designed using Fusion 360 software (Autodesk) and included i) the chip [50 mm (length) x 1 mm (width) x 0.02 mm (height)] and ii) mVWP structures [0.1, 0.2, or 0.8 mm (Wing length) ×

0.3 mm (width) × 0.02 mm (height)] to adjust the flow blockage ratio (0, 20, or 80 %) by modifying the Wing length. The molds were produced by casting a mixture of PDMS elastomer base and curing agent (10:1 wt/wt) upon heat curing at 60°C for 4 h in the dry oven. The PDMS molds were used to cast polymer solution via UV-crosslinking (365 nm, 265 mJ cm^{-1}, UV Crosslinker) for 200 s, followed by distilled water washing and vacuum drying at room temperature for 24 h. The mVWP was stained with Sudan Black B solution (0.3 %, wt/vol) in water and ethanol (30:70 vol/vol, Sigma Aldrich).

Flow and hemostasis: The chip channels were conditioned to induce platelet responses like an injury with EC dysfunction in blood vessels. Hence, i) as a model of basement membrane, the channels were coated with rat collagen type I (200 μg mL^{-1} in 0.1 M acetic acid, Sigma Aldrich) by incubating them for 1 h. The samples were then washed using Tyrode's buffer (Sigma Aldrich) with 10 mM HEPES, 2.7 mM KCl, and 137 mM NaCl. ii) As a model of EC dysfunction to recruit platelets, human von Willebrand factor (vWF, 10 μg mL^{-1}, Sigma Aldrich) in the washing buffer was injected into the chip channels and incubated overnight, followed by washing again.

Next, mVWP was placed into the PDMS chip along the flow direction. The bottom of the chip was bonded to a glass slide upon plasma treatment using an instrument (PDC-32G-2, Harrick Plasma) for 60 s. In the chip, each of the inlet and outlet ports were connected to a 19-gauge blunt needle (Korea Vaccine) via silicone tubing (inner diameter: 1 mm, KoreaAceScientific). The inlet silicone tube was connected to a syringe in a pump (PHD ULTRA, Harvard Apparatus) so that whole blood could be injected at a shear rate of 860 s^{-1} for 2 min, monitored by optical microscopy (Leica DMi8, Leica Microsystems). The calcium signal was examined by collecting blood in heparin tubes, incubation with Fluo-4 AM (10 μM, Invitrogen) for 30 min at 37°C, and confocal imaging (LSM 780, Zeiss) of calcium flux. The role of vWF in platelet activation was determined by pre-incubating whole blood with an antibody to CD42b (1:500 dilution, rabbit anti-mouse, A10113, ABclonal) to inhibit interaction between vWF and the GPIbα receptor.

Immunofluorescence staining: After removing residual blood, the chip was washed using Tyrode's buffer (see above) and fixed in 4 % (vol/vol) paraformaldehyde (CellNest) for 20 min. The chip was then washed three times with 1 × phosphate buffered saline (PBS, Welgene) and blocked with 5 % (wt/vol) bovine serum albumin (GenDEPOT) in 1 × PBS. Next, the chip was incubated overnight at 4°C with primary antibodies including CD42b (1:500, rabbit anti-mouse, A10113, ABclonal) and CD62p (1:50, rat anti-mouse, 550289, BD Biosciences). The chip was washed with 1 × PBS and treated at room temperature for 1 h with secondary antibodies including Alexa Fluor 488 (1:500, goat anti-rabbit, 111-545-003, Jackson ImmunoResearch) and Alexa Fluor 594 (1:500, donkey anti-rat, 712-585-150, Jackson ImmunoResearch) in addition to Alexa Fluor 647 Phalloidin (1:400, A22287, Thermo Fisher Scientific). After washing three times with 1 × PBS, platelet aggregation was visualized using confocal imaging (LSM980, Zeiss) and quantified using ImageJ software (Fiji).

2.8. Whole blood perfusion test

i) In vitro phantom model of thoracic of aorta: A silicone tube (ID: 8 mm, OD: 10 mm) was used as a phantom model of the thoracic aorta, and 6-mm punctures were created using a biopsy punch (Acu-Punch). The puncture sites were coated with rat collagen type I (200 μg mL^{-1} in 0.1 M acetic acid, Sigma Aldrich) by 1 h incubation, followed by washing with Tyrode's buffer (Sigma Aldrich) including 10 mM HEPES, 2.7 mM KCl, and 137 mM NaCl. Human von Willebrand factor (vWF, 10 μg mL^{-1}, Sigma Aldrich) was dissolved in Tyrode's buffer, and sprayed around the puncture sites with overnight reaction to facilitate platelet adhesion. After washing, VWP groups [SL(+) with flat Wing, SL(+) HC (+), and SL(+) with bump Wing] were deployed into the punctures, which were then subjected to perfusion of porcine whole blood at a 750 mL min^{-1} for 5 min using a peristaltic pump (BT100L, LeadFluid, Hebei, China). Platelets adhesion was imaged by FE-SEM (Merlin, Zeiss) and quantified using ImageJ software (Fiji).

ii) Ex vivo porcine carotid artery: As a mimetic clinical model, porcine carotid arteries (ID: 3 mm, OD: 5 mm) were punctured (8 Fr: 2.67 mm) using a biopsy device (Acu-Punch), followed by deployment of commercial VCD devices (suture-based, membrane-based, and PEG-based) as well as VWP. The arteries with devices were placed in a customized reactor and perfused with porcine whole blood at a 750 mL min^{-1} for 5 min using a peristaltic pump (BT100L). Platelet adhesion was imaged by FE-SEM (Merlin) and quantified using ImageJ software (Fiji).

2.9. Porcine aorta model

Animal and experimental group: All pig experiments were conducted in accordance with the IACUC (approval number: 2024-0296). Yorkshire pigs (40 kg, male, XP Bio) were acclimatized in an animal facility for at least 1 week before surgery. Anesthesia was induced by intramuscular injection of Zoletil (50 mg kg^{-1}, Virbac Korea) and xylazine (5 mg kg^{-1}, Rompun, Bayer Korea) and maintained with isoflurane (2–2.5 % (vol/vol), Hana Pharm) via endotracheal inhalation.

The porcine model of vascular closure was set with the first four groups (N = 3 each) for immediate sacrifice as follows. Group 1 [VWP with neither self-locking (SL) nor hemodynamic control: HC) [SL(−) HC (−)], Group 2 [VWP with SL and flat Wing: SL(+) w/flat Wing], Group 3 [VWP with SL and HC: SL(+) HC(+)], Group 4 [VWP with SL and bump Wing: SL(+) w/bump Wing]. The second experiment for 30-day survival examines the comparison of VWP [SL(+) HC(+)] with suture closing (N = 3 each).

Surgery: Pressure monitoring was set up by incising the thoracic wall after exposing the thoracic aorta through sequential incisions from the subcutaneous tissue to the intercostal muscles. Sodium heparin (100 IU kg^{-1}, JW Pharmaceutical) was administered intravenously. Two single-lumen pediatric central venous catheters (ES-04150, Teleflex) were inserted into the descending aorta and the femoral artery, each connected to a pressure transducer (TruWave™3, PX260, Edwards Lifesciences) and monitoring system (CARESCAPE B450 Monitor, GE healthcare). The transducer was positioned at heart level, zeroed to atmospheric pressure, and used to monitor proximal and distal arterial pressure curves. Systolic blood pressure (SBP), diastolic blood pressure (DBP), and mean arterial pressure (MAP) were continuously recorded. Arterial pressure lines (A-lines) were periodically flushed with 0.9 % (wt/vol) saline (Dai Han Pharm) to maintain patency.

Each aortic puncture was created by first clamping the descending and distal thoracic aorta to temporarily block blood flow. Guidewires and dilators of varying sizes [9 Fr (SI11142, Teleflex) and 18 Fr (G01328, Cook Medical)] were then used to generate the puncture for VWP deployment.

As the first experiment set for immediate sacrifice, the VWP was inserted into the puncture site, and shape recovery of the device was induced by treating it with 45°C warm saline. During vascular closure, the surgical grade was evaluated using the bleeding scoring system, and the time to hemostasis was recorded. After closure, changes in pressure parameters and the time required to reach arterial pressure equilibrium were assessed using arterial pressure monitoring. The pressure gradient was calculated once the proximal and distal pressures reached a plateau for at least 5 s with a consistent difference between the two measurements.

As the second experiment set for 30 days survival, vascular punctures were closed using 5-0 polypropylene suture (PROLENE™, Ethicon Inc.) in comparison with VWP [SL(+) HC(+)] deployment. Each puncture site was marked with a LigaClip (Ethicon Inc.) to facilitate angiography. Soft tissues and skin were closed using 1-0 polyglactin 910 suture (VICRYL™, Ethicon Inc.) and skin staples (Visistat 35W, Teleflex), followed by a 30 day monitoring period. Pain was managed with oral injection of meloxicam (0.5 mg kg^{-1}, Medica Korea) daily for 7 days, and infection was prevented with oral enrofloxacin (10 mg kg^{-1}, CityBio).

Pigs were euthanized by intravenous bolus injection of potassium chloride (20 mg kg^{-1}, JW Pharmaceutical), and tissue samples from the surgical site were collected for histological analysis.

Angiography: Blood flow patency was assessed by angiography (C-arm radiography system, OEC Series 9600, GE Healthcare) 4 weeks after surgery. A 5 Fr vascular sheath (Supersheath, Medikit) was inserted into the femoral artery, followed by injection of a nonionic contrast medium (Visipaque 320, GE Healthcare). The pigs were then euthanized, and thoracic aortas were collected for histological analysis.

Histology: Endothelialization of porcine thoracic aorta after puncture closure by suturing or VWP was evaluated by hematoxylin and eosin (H&E) and Verhoeff's Van Gieson (VVG) staining following the manufacturer's instructions. Tissues were fixed in 4 % (vol/vol) paraformaldehyde (CellNest) overnight at 4°C, embedded in paraffin, and sectioned at 4 μm thickness using a microtome (Leica Microsystems). Sections were deparaffinized in xylene and rehydrated through graded ethanol solutions (100 %, 95 %, 80 %, 70 %) diluted with deionized water. Antigen retrieval was performed by heating in citrate buffer (10 mM, pH 6.0, Sigma Aldrich) for 40 min at 95°C. Sections were permeabilized with 0.1 % Triton X-100 (PBST, Sigma Aldrich) in PBS for 30 min, followed by blocking with 1 % bovine serum albumin (GenDEPOT) in PBST for 1 h at room temperature. Primary antibodies against CD41 (1:100, 24552-1-AP, proteintech), fibrinogen (1:100, ab232793, Abcam), CD31 (1:100, sc-376764, Santa Cruz Biotechnology), CD68 (1:100, ab125212, Abcam), and ARG-1 (1:200, LS-C447907, LSBio) were applied overnight at 4°C. After washing with PBS, the sections were incubated with secondary antibodies including Goat anti-rabbit Alexa Fluor 594 (1:1000, 111-545-003, Jackson Immuno Research, West Grove, PA, USA) for 2 h in the dark. Nuclei were counterstained with NucBlue Live Ready Probes Reagent (R37605, Invitrogen), followed by confocal imaging (LSM 780, Zeiss, Oberkochen, Land Baden-Württemberg, Germany) with quantitative analyses using ImageJ (Fiji). Angiogensis of adventitia was determined through optical imaging of porcine thoracic aorta with subsequent treatment of CD31 primary antibody. After PBS washing, sections were incubated with HRP-labeled secondary antibody (anti-mouse polymer, K4001, Agilent Dako) for 20 min at room temperature. Color development was performed with DAB substrate (K3468, Agilent Dako) for 5 min. Sections were rinsed with deionized water and counterstained with hematoxylin (K8008, Agilent Dako). Endothelialization was assessed by CD31-positive staining using optical imaging. Hemostasis levels were evaluated by measuring neointima area and vascular wall repair around the puncture site using a Thunder imaging system (Leica Microsystems) and quantified with ImageJ (Fiji).

Real-time-polymerase chain reaction (qPCR): Target marker genes were identified to determine thrombotic feature (vWF, PF-4, and P-sel), macrophages (CD68 and MCP1), and M2 (ARG-1, IL-10, TGF-β) polarization of macrophages, and angiogenesis (CD31 and CD34). Total RNA was extracted using an RNA extraction kit for FFPE samples (AM1975, Invitrogen, California USA), following the manufacturer's instructions. RNA concentration was measured using a NanoDrop 2000 Spectrophotometer (Thermo Fisher) with nuclease-free water (Thermo Fisher). The RNA was converted to complementary deoxyribose nucleic acid (cDNA) using AccuPower CycleScript RT Premix (K2004, Bioneer, Seoul, Republic of Korea) and T-100 Thermal Cycler (Bio-Rad, CA, USA) following the manufacturer's instructions. The cDNA was mixed with specific primers (Table S5) and SYBR Green PCR Master Mix (Applied Biosystems, Waltham, MA, USA), and amplification was performed on a StepOne Plus RT PCR System (Applied Biosystems). The expression of glyceraldehyde-3-phosphate dehydrogenase (GAPDH) was used as an endogenous control, and the relative gene expression was calculated with $2^{-\Delta\Delta Ct}$ values.

2.10. Statistical analysis

Data are presented as mean ± standard deviation (SD), with "N" indicating the number of independent biological samples. Each experiment was repeated at least three times. Pairwise comparisons were performed using unpaired Student's t-tests, and multiple-group comparisons were conducted using one-way ANOVA with Tukey's post-hoc test. Statistical significance was defined as $p < 0.05$, with annotations (*$p < 0.05$, **$p < 0.01$, ***$p < 0.001$, ns: not significant). Analyses were performed using Origin 2018 (OriginLab) and GraphPad Prism 10 (Dotmatics).

3. Results

3.1. VWP programming to operate auto-plugging with hemostatic sealing

When the catheter is removed from the blood vessel (Fig. 1a), the large-bore puncture (≥15 Fr) presents a clinical challenge due to bleeding, hematoma, and thrombosis [16,17]. To address this, i) the memory-programmable VWP is proposed as a translatable solution by assembling the Ring into a single structure with the Body and Wing, and ii) each structure is programmed to memorize a unique shape change so that self-locking (Ring and Body) and hemodynamic control (Wing) can be coordinated to enable automated plugging (self-locking) and hemostatic sealing (hemostatic control). First, the VWP structure is designed by determining the size of each part (Ring, Body, and Wing) after (top) and before (bottom) shape recovery (Fig. S1a). Then, prototypes of VWP parts matching the design are produced using a 3D-printed master mold (top) and SMPs (bottom, Fig. S1b).

The step-by-step procedure for each functional step is shown schematically (Fig. 1b). In the self-locking step, Ring squeezing (blue arrow) and Body expansion (green arrow) act together to close the puncture through tight plugging. Under blood flow, platelets encounter the curved Wing (yellow) due to flow blockage, and the resulting increase in shear rate induces platelet aggregation and activation. In this way, hemostatic sealing enables leakage-free closure. In the hemodynamic control step, the curved Wing recovers to a flattened state (yellow arrow), preventing further thrombosis and reducing the risk of vessel occlusion by preserving laminar blood flow.

Shape recovery-based easy plugging of the VWP is demonstrated in a thoracic aorta phantom model during catheter and sheath delivery following a clinical scenario (Fig. 1c and Video S1). A silicone-tube thoracic phantom with continuous flow is used, followed by creating a 6-mm puncture. Following the clinic-mimetic procedure using temporary shapes of the three VWP parts, a sheath is placed over the puncture site, and a catheter is pushed inside the sheath to position the Body and Wing. The Ring is advanced through the space between the sheath and catheter using pusher 2, after which the catheter and pusher are removed. Next, the Body and Wing are advanced into the puncture using pusher 1 while the thread is pulled out, stabilizing their position for plugging. Finally, 45°C saline is injected through the sheath to trigger shape recovery of all three VWP parts, and the disappearance of water leakage confirms complete plugging.

As an additional assessment of reproducibility, the three VWP parts (Ring, Body, and Wing) undergo five cycles of shape programming after forming temporary shapes by compressing the Body by 25 %, folding the Wing at 90°, and stretching the Ring by 50 %, 100 %, and 150 % (Fig. S2). Shape recovery is triggered by exposure to 45°C water flow from a syringe at 2.0 mL s^{-1} for 15 s, consistent with the SMP/PCL(95/5) recovery time. The fixity and recovery ratios of angle (Wing) and diameter (Body and Ring) remain consistently above 90 % except for Ring stretching at 150 % strain across all five cycles (Fig. 1d). These results indicate recycling potential of SMP/PCL(95/5) with 100 % Ring stretching for up to five cycles without loss of shape memory function. Additionally, low standard deviations among three independent samples support batch-to-batch reproducibility.

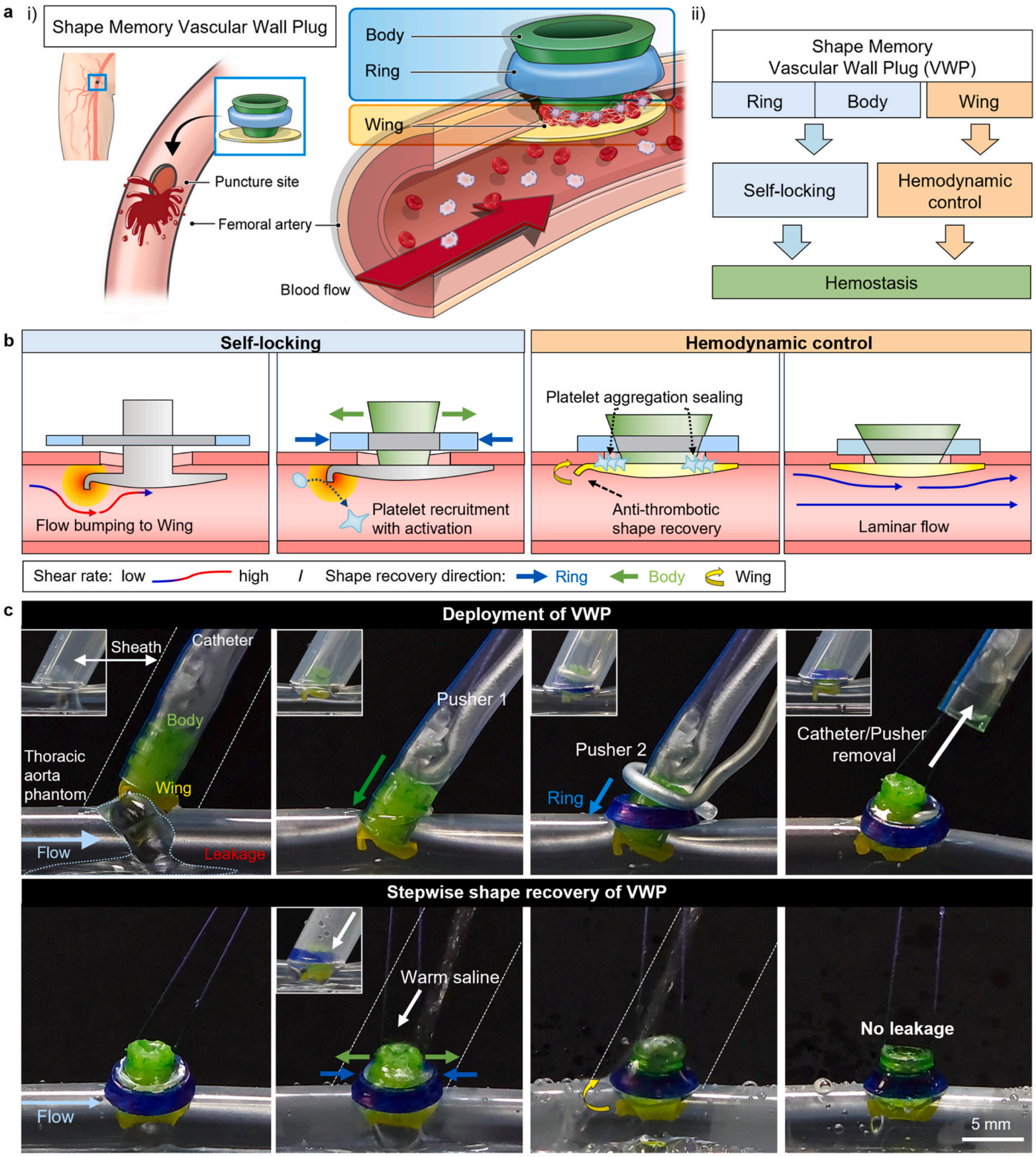

Thoracic aorta phantom: OD: 10 mm, ID: 8 mm, Flow rate: 0.25 m/s, Inset images represent deployment with sheath.

d

	Deformation	Strain (%)	R_f (%) (N=3)			R_r (%) (N=3)		
			Cycle 1	Cycle 3	Cycle 5	Cycle 1	Cycle 3	Cycle 5
Body	Compression	25%	100.13±0.58	96.50±0.19	99.37±0.49	99.82±0.65	99.97±1.36	99.91±0.39
Wing	90° Fold	90°	100.07±0.05	99.14±0.12	99.76±0.20	99.89±0.05	99.98±0.05	100.04±0.08
Ring	Stretch	**50**	98.07±4.44	97.74±1.51	97.66±0.99	99.53±1.30	100.11±0.28	99.95±1.21
		100	98.55±1.53	95.86±0.24	90.10±3.72	99.80±0.87	99.38±1.54	99.77±0.46
		150	93.48±7.18	89.05±9.00	79.33±3.57	99.73±0.12	99.85±0.92	98.67±0.70

R_f: Shape fixity ratio, R_r: Shape recovery ratio

(caption on next page)

Fig. 1. Self-locking and hemodynamic control as key to multi-part memory programming in vascular wall plug (VWP) to enable auto-plugging with hemostatic sealing. a, Following catheter removal from the femoral artery, a large-bore puncture (≥15 Fr) presents a clinical challenge due to bleeding, hematoma, and thrombosis. Therefore, i) a new concept of VWP is proposed as a solution by operating the Ring, Body, and Wing parts. ii) Each of these three parts is programmed to memorize a unique shape change so that self-locking (Ring and Body) and hemodynamic control (Wing) can be operated to enable auto-plugging with hemostatic sealing. **b**, The step-by-step procedure to operate the function of each part is shown schematically (Fig. 1b). In the self-locking step, collaboration of Ring squeezing (blue arrow) and Body expansion (green arrow) closes the puncture by tight plugging. Platelets bump the curved Wing (yellow) under blood flow due to flow blockage, and the incremental shear rate induces aggregation and activation of platelets. This hemostasis sealing enables leakage-free closure of the puncture. In the hemodynamic control step, the curved Wing recovers to a flattened shape (yellow arrow) so that further thrombosis is prevented and the risk of vessel occlusion is removed by preserving laminar blood flow. **c**, As a phantom model of the thoracic aorta, a silicone tube is used to generate continuous flow, followed by punching to generate a 6 mm puncture. Using temporary shapes of the three VWP parts, Body is penetrated with thread to stabilize its position through the puncture site. Body is seized at the end of the catheter to control Wing deployment into the puncture, and Ring is placed outside the catheter to tag onto Body using a pusher. As a clinic-mimetic procedure, i) a sheath is placed onto the puncture site; ii) a catheter is pushed inside the sheath to place Body and Wing into the puncture; iii) Ring is pushed through the space between the sheath and catheter using pusher 2; iv) Body and Wing are pushed into the puncture using pusher 1 while the thread is pulled out so that Body and Wing are stably positioned for plugging; v) the catheter and pushers are removed; and vi) 45°C saline is flowed through the sheath using a syringe at 2.0 mL s^{-1} for 15 s to trigger shape recovery of the three VWP parts. Plugging status is confirmed by verifying the disappearance of water leakage. **d**, The three parts (Ring, Body, and Wing) of VWP undergo 5 cycles of shape programming after producing temporary shapes by compressing Body by 25 %, folding Wing at 90°, and stretching Ring by 50, 100, and 150 %. Shape recovery of each part is triggered by exposure to 45°C water at a flow rate of 2.0 mL s^{-1} for 15 s. Fixity and recovery ratios of angle (Wing) and diameter (Body and Ring) remain consistently above 90 % except for 150 % strain of Ring across all 5 cycles (bottom table). These results indicate recycling potential of SMP/PCL(95/5) with 100 % Ring stretching up to five times without loss of shape memory function. The low standard deviations from three independent samples demonstrate batch-to-batch reproducibility.

3.2. *Polymer blending and strain control of self-locking to resist high burst pressure*

The 6-arm SMP (x% PCL-co-y% PGMA) is synthesized via ring-opening polymerization of ε-caprolactone (CL) and glycidyl methacrylate (GMA) monomers (Fig. S3a). The synthesis is validated by characterizing i) the polymer structure with a ^{1}H NMR spectrum in $CDCl_3$, which shows peaks at $\delta = 6.13$ [s, $=CH_2$, (G2)], 5.58 [s, $=CH_2$, (G1)], 4.10 [m, $-OCH_2$, (A)], 2.41 [m, $-CH_2$, (E)], 1.97 [s, $-CH_3$, (F)], and 1.74 [m, $-CH_2$, (B)], 1.45 [m, $-CH_2$ (D)] (Fig. S3b). ii), the composition of the 6-arm SMP by Fourier transform infrared (FTIR) spectroscopy with characteristic spectra peaks. SMP/PCL samples (100/0, 95/5, and 90/10) are exposed to ethylene oxide (EO) gas for sterilization (Fig. S3d). When chemical structures before and after sterilization are assessed by ^{1}H NMR, no significant degradation or peak shift is observed, indicating EO sterilization stability of the SMP/PCL samples. Cell viability is also unchanged before and after EO sterilization of SMP/PCL(95/5), confirming maintained biocompatibility (Fig. S3e).

The results of i) synergistic frequency sweeps and ii) high-cycle fatigue testing confirm viscoelastic stability of the 6-arm SMP under continuous aortic contraction (Fig. S4a). As an indication of long-term stability, accelerated degradation of SMP is evaluated following ASTM F1980 (Fig. S4b). Based on calculations, weight loss at 70 ± 2°C for 37, 74, or 111 days corresponds to 1, 2, or 3years of real-time degradation. SMP samples (diameter: 6 mm, thickness: 500 μm) are incubated in PBS (pH 7.4) at 70 ± 2°C with weight measurements at day 0 (initial), 37, 74, and 111 (final). Weight-loss analysis shows that SMP maintains over 65 % weight until the 2-years equivalent (35 % loss) and undergoes complete degradation by the 3-years equivalent. These results indicate functional and structural maintenance of the SMP for approximately 2 years.

Thermomechanical analysis of three compositions (SMP/PCL: 100/0, 95/5, and 90/10) is carried out using DMA under controlled cyclic stress for five consecutive cycles (Fig. S5). SMP/PCL(95/5) shows over 95 % R_f and 99 % R_r across all cycles, whereas increased PCL content reduces efficiency (Fig. 2a, left). To avoid tissue damage, the triggering temperature (45°C) is validated against 39°C and 42°C by comparing recovery times of each film composition (Fig. 2a, right). Shape recovery is triggered by syringe flow at 2.0 mL s^{-1}, identical to the phantom experiment. Higher triggering temperatures reduce recovery time. Although increasing PCL ratio slows recovery, SMP/PCL(95/5) recovers within 15 s even at 39°C. Together, triggering at 45°C with recovery within 15 s supports safe and efficient clinical operation of the VWP [35].

Stress–strain analysis shows that the 95 % 6-arm SMP blended with 5 % PCL has the highest elastic modulus and toughness among the blends (Fig. 2b–i). When the modulus (slope) and toughness (area) of each blend are compared to 100 % SMP, the toughness-enhancing effect of 5 % PCL is diminished in the 90/10 blend. Relative to the 100/0 and 90/10 blends, the 95/5 blend maintains a higher shape recovery force during strain elevation from 0 to 150 % tensile (left) and up to 10 % compression (right) (Fig. 2b–ii). Thus, the 95/5 ratio is selected and justified for subsequent experiments. Thermal analysis of SMP blends shows increasing crystallinity (χ_c) with increasing PCL content (Table 1). However, when PCL content increases from 0 to 10 % (Fig. 2c), distinct phase separation appears only in the 90/10 blend—shown as black/white contrast by SEM and blue/red contrast by AFM—with a significant increase in surface roughness (Fig. S3c). These findings further support the choice of the 95/5 blend ratio.

Shape recovery force of SMP is evaluated under varying tensile strains using maximum loading (Fig. S6a). In the test procedure, both ends of each SMP film are fixed to define the original shape, then the film is stretched under heat to allow chain mobility. After cooling to fix the elongated temporary shape, the film is reheated above its melting temperature to generate recovery force and lift the load. At 50 % strain with a 200 g load (Fig. S6b), the film fails to fully recover. At 100 % strain with a 220 g load, the film shows maximum recovery force, pulling the weight above the original line; however, at 150 % strain, only 200 g is lifted.

For the SMP/PCL(95/5) blend (Fig. 2d and Fig. S6c), 100 % Ring strain—from circumferential enlargement to squeezing—yields higher burst pressure than 50 % or 150 % strain, as confirmed quantitatively. In the ex vivo burst-pressure test (Fig. S6d), a porcine carotid artery (diameter: 3.5 mm) is harvested and integrated into a flow system under pressure monitoring. After puncturing the arterial wall (9 Fr, 3 mm diameter) and closing it with the VWP, burst pressure with (+) or without (−) self-locking is measured during pressure elevation. Without self-locking (−), rapid and heavy leakage occurs (left), whereas with self-locking (+), visible closure is maintained until burst (right). The average burst pressure with self-locking (+) is more than five-fold higher than without self-locking (−).

3.3. *Blood microfluidics with CFD to examine flow blockage and platelet responses*

Mouse whole blood is perfused into a microfluidic chip as an in vitro model of vascular puncture (Fig. 3a). The curved Wing of the miniature VWP (mVWP) is coated with vWF to mediate platelet aggregation through vWF–GPIb signaling [28–30]. The mVWP is deployed into the microfluidic channel so that blood platelets aggregate on the Wing and become activated via Ca^{2+} induction following shear gradients generated by partial flow blockage. In the CFD simulation of microfluidic

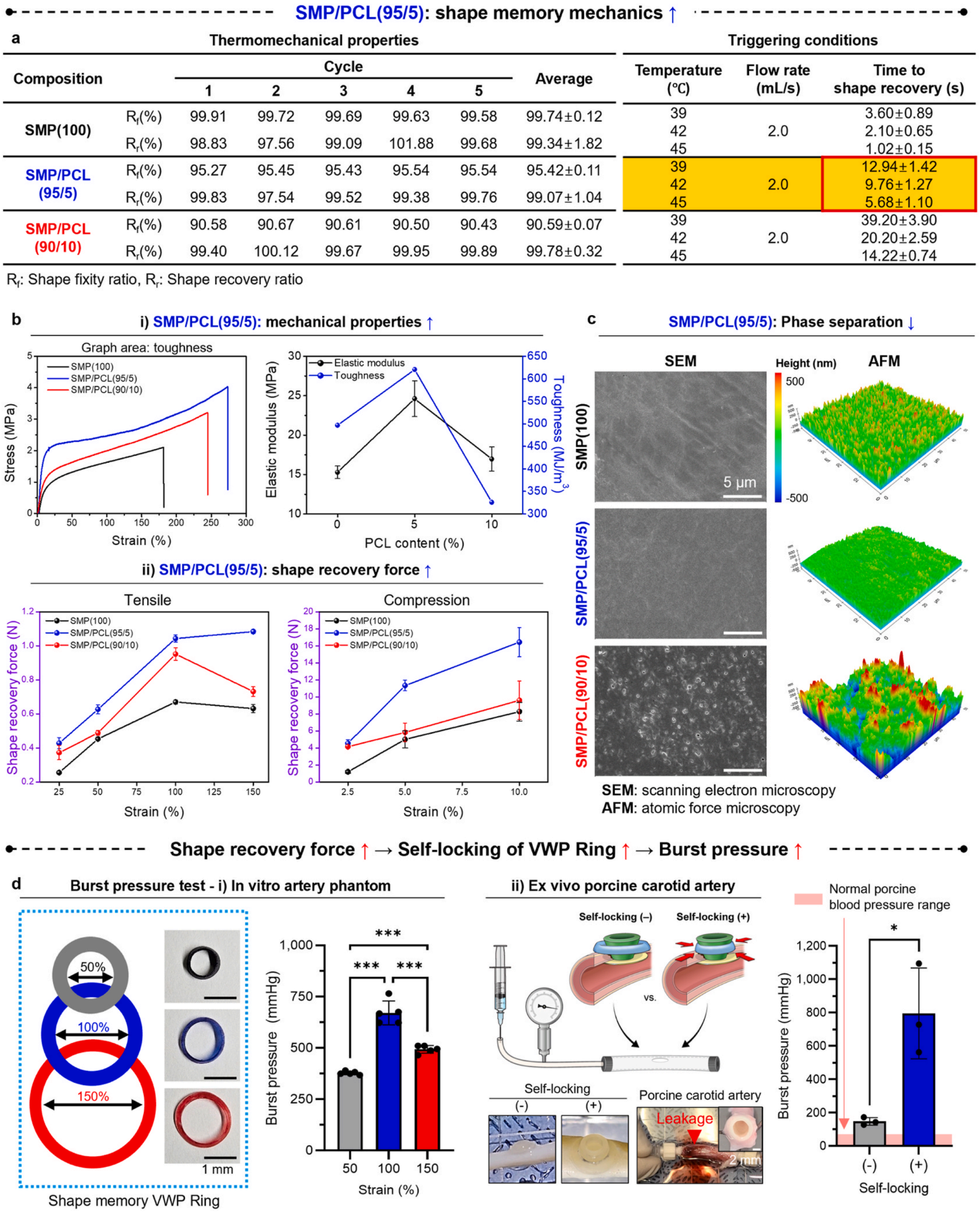

SMP/PCL(95/5): shape memory mechanics ↑

a Thermomechanical properties

Composition		Cycle 1	2	3	4	5	Average
SMP(100)	R_f(%)	99.91	99.72	99.69	99.63	99.58	99.74±0.12
	R_r(%)	98.83	97.56	99.09	101.88	99.68	99.34±1.82
SMP/PCL (95/5)	R_f(%)	95.27	95.45	95.43	95.54	95.54	95.42±0.11
	R_r(%)	99.83	97.54	99.52	99.38	99.76	99.07±1.04
SMP/PCL (90/10)	R_f(%)	90.58	90.67	90.61	90.50	90.43	90.59±0.07
	R_r(%)	99.40	100.12	99.67	99.95	99.89	99.78±0.32

Triggering conditions

Composition	Temperature (°C)	Flow rate (mL/s)	Time to shape recovery (s)
SMP(100)	39	2.0	3.60±0.89
	42		2.10±0.65
	45		1.02±0.15
SMP/PCL (95/5)	39	2.0	12.94±1.42
	42		9.76±1.27
	45		5.68±1.10
SMP/PCL (90/10)	39	2.0	39.20±3.90
	42		20.20±2.59
	45		14.22±0.74

R_f: Shape fixity ratio, R_r: Shape recovery ratio

Fig. 2. Polymer blending and strain control of self-locking as handling keys of high burst pressure. a, (left) Thermomechanical analysis of three compositions (SMP/PCL: 100/0, 95/5, and 90/10) is carried out using DMA under controlled cyclic stress for five consecutive cycles, and the shape memory efficiency is determined by calculating the shape recovery ratio (R_r) and shape fixity ratio (R_f). SMP/PCL(95/5) exhibits over 95 % R_f and 99 % R_r through the 5 cycles, although an incremental PCL ratio decreases the efficiency. (right) In a range to prevent tissue damage, the triggering temperature (45°C) is justified in comparison with 39°C and 42°C by examining the recovery time of each test film using the three different compositions. Although the incremental ratio of PCL blending slows down the shape recovery time, the SMP/PCL(95/5) undergoes the shape recovery within 15 s even at 39°C. **b,** Each blend in the stress-strain curve is compared to 100 % SMP. The PCL role in 95/5 improves the slope (elastic modulus) and graph area (toughness) more than in 90/10. The analysis of the stress-strain curve shows the maximum elastic modulus and toughness of 95 % 6-arm SMP blended with 5 % PCL compared to the other 6-arm SMP/PCL blends. Data are shown as mean ± SD, N = 3 independent replicates. Compared to the 100/0 and 90/10 blending ratios of SMP to PCL during strain elevation, the 95/5 blend maintains higher shape recovery force without reduction from 0 to 150 % tensile (left) and 10 % compression (right) conditions. **c,** As the blending ratio of PCL to SMP increases from 0 to 10 %, either the black and white features under scanning electron microscopy (SEM) or the blue and red features under atomic force microscopy (AFM) appear only at 90/10, indicating clear phase separation between SMP and PCL. Hence, the choice of the 95/5 ratio is justified for the other experiments. **d,** In the 95/5 blending ratio of SMP to PCL, i) a 100 % strain of Ring from circumferential enlargement to squeezing serves as a key factor to handle high burst pressure compared to 50 and 150 % strain (Scale bar = 1 mm), as confirmed by the quantitative analyses. ii) Each porcine carotid artery (diameter: 3.5 mm) is harvested and placed into a flow system under pressure monitoring as illustrated. When the artery wall is punctured (9 Fr, 3 mm diameter) and closed by VWP, the burst pressure with (+) or without (−) operation of self-locking is examined by elevating flow pressure. During pressure elevation, self-locking (−) exhibits fast and heavy leakage (left) in contrast to efficient visible closure (right) of self-locking (+) until reaching the burst threshold (bottom) (Scale bar = 2 mm). The average burst pressure of self-locking (+) is over five-fold higher than that of self-locking (−). Data are shown as mean ± SD, N = 3 biological replicates.

Table 1
Thermal properties of polymers.

	T_c (°C)	T_{m1} (°C)	T_{m2} (°C)	ΔH_c (J g^{-1})	ΔH_m (J g^{-1})	χ_c (%)	$\lambda_{25^\circ C}$ (W m^{-1} K^{-1})	$\lambda_{37^\circ C}$ (W m^{-1} K^{-1})
SMP (100)	−1.45	36.74	–	36.59	39.75	26.23	0.227	0.506
SMP/PCL (95/5)	9.52	38.47	53.26	39.05	47.09	27.99	0.342	0.507
SMP/PCL (90/10)	17.43	39.16	54.01	41.18	46.78	29.52	0.269	0.368
PCL (100)	20.71	–	58.37	49.67	60.20	35.61	0.171	0.188

T_c: Crystallization temperature (°C).
T_{m1}: Melting temperature of SMP (°C).
T_{m2}: Melting temperature of PCL (°C).
ΔH_c: Crystallization enthalpy (J g^{-1}).
ΔH_m: Melting enthalpy (J g^{-1}).
χ_c: $\Delta H_{c,\ sample}$ relative to $\Delta H_{c,\ 100\ \%\ PCL}$ (139.5 J g^{-1}) (%).
$\lambda_{25^\circ C}$: Thermal conductivity at 25 °C (W m^{-1} K^{-1}).
$\lambda_{37^\circ C}$: Thermal conductivity at 37 °C (W m^{-1} K^{-1}).

chips, with velocity distributions visualized by color changes (Fig. 3b and Fig. S7a–b), velocity gradients become more apparent as the initial velocity (v_i) increases from 9 to 18 and further to 36 mm s^{-1} and/or the flow blockage ratio increases from 20 to 80 %. The gradient and maximum value of shear rate ($\dot{\gamma}$) also becomes more incremental following the increases of initial shear rate ($\dot{\gamma}_i$: 430, 860, and 1730 s^{-1}) and/or the flow blockage ratio (20 and 80 %). After shape recovery of the Wing—from 20 % or 80 % blockage (curved) back to 0 % (flat)—the lumen appears cleared under confocal microscopy (Fig. 3c). The two blockage ratios show no significant difference in intracellular calcium flux, as both maintain higher activation levels compared to 0 % blockage (Fig. 3d). Based on this, a 20 % blockage ratio is selected for subsequent experiments.

As a mechanistic insight into the first step (Fig. S8a), platelets bump onto the curved Wing while the VWP is positioned on the vascular wall through Ring locking and Body plugging. Flow blockage by the curved Wing induces platelet recruitment and adhesion via vWF (under the ECs)–GPIb (on platelets) binding to stop bleeding. Platelet activation then induces fibrinogen clustering through GPIIb/IIIa engagement to complete hemostasis. Photographic and fluorescence images with quantitative analysis show that 20 % blockage by the curved Wing [inhibitor (−)] significantly increases platelet adhesion (GPIb, green) and activation (P-selectin, red) compared to the recovered (flat) condition (Fig. 3e–f and Fig. S8–9). Inhibition of vWF–GPIb interaction [inhibitor (+)] significantly reduces blockage-induced platelet responses to flat-level values, demonstrating the mechanistic role of vWF–GPIb signaling in mediating platelet responses under 20 % flow blockage.

3.4. 18 Fr puncture closure of porcine aorta using VWP

A harsh model for deploying large-diameter catheters is established as follows (Fig. 4a). An 18 Fr puncture is created in the wall of the porcine thoracic aorta (diameter: 10 mm), and a size-matched VWP is deployed while monitoring proximal and distal blood pressures. The experimental groups are designed to first examine memory programming of self-locking (SL) through coordinated Ring squeezing and Body expansion to tightly block the puncture. The Wing then undergoes shape recovery from curved to flat as the hemodynamic control (HC) step, managing thrombosis and laminar flow under support from SL. Without recovery, the curved Wing is expected to induce excessive thrombosis. A total of 12 pigs (N = 12) are used for immediate sacrifice after deployment in four groups (N = 3 each). Group 1 [SL(−) HC(−)] represents no memory-programming effects. Group 2 [SL(+) w/flat Wing] incorporates Body and Ring actions but lacks hemostatic sealing because the Wing is kept flat. Group 3 [SL(+) HC(+)] possesses the complete memory effects of all three parts. Group 4 [SL(+) w/bump Wing] is expected to show excessive thrombosis due to the unrecovered curved Wing, while maintaining SL function. Each group is illustrated schematically (Fig. 4b).

Reference pressure characteristics from clinical monitoring are shown in Fig. 4c. Under bleeding conditions, the proximal site shows a normal sinusoidal waveform, whereas the distal waveform is dampened by low pressure (left). Hemostatic closure preserves similar high-level sinusoidal waveforms at both sites (middle). Excessive thrombosis does not alter waveform morphology but markedly reduces distal pressure relative to proximal (right). These pressure changes are further explained by CFD simulations calculating pressure drops caused by intraluminal thrombus (Fig. S10). As thrombus accumulates on the intima of the thoracic aorta (diameter: 10 mm), luminal obstruction is modeled at 10 %, 25 %, and 50 % using a cylindrical tube. With the proximal, thrombus, and distal sites defined and a blood-flow velocity of 1.0 m s^{-1} applied, the pressure gradient becomes progressively greater as obstruction increases. From proximal to distal ends, the pressure drop reaches 1.4, 1.7, and 4.5 mmHg at 10 %, 25 %, and 50 % obstruction, respectively.

As a preclinical model reflecting inter-patient blood pressure variation, pig blood pressure is recorded before and after deployment across the four device groups [SL(−) HC(−), SL(+) with flat Wing, SL(+) HC (+), SL(+) with bump Wing] (Table S1). Regardless of condition, systolic and diastolic pressures remain within non-pathological ranges, supporting the reliability of this preclinical model for evaluating VWP function. After blood reperfusion by removal of a vascular clamp (Fig. 4d and Fig. S13), only Group 3 [SL(+) HC(+)] achieves hemostatic closure upon flow stabilization, defined as a 5-s plateau in both proximal and distal pressures. Group 4 [SL(+) w/bump Wing] demonstrates a pattern of excessive thrombosis. H&E staining shows bleeding in Group 1, indicating incomplete closure, versus moderate, minimal, and dense thrombotic features in Groups 2, 3, and 4, respectively, which is further supported by signals of activated platelets (green, CD41-positive) and fibrinogen (red) (Fig. 4e). Compared to Group 1 [SL(−) HC(−)] and Group 2 [SL(+) w/flat Wing], Group 3 [SL(+) HC(+)] exhibits the fastest (i) hemostasis and (ii) equilibration of arterial pressure, indicating the most efficient hemostatic handling, consistent with the lowest surgical grade (Fig. 4f and Table S2–4). These outcomes in Group 3 result in (i) the smallest proximal–distal pressure difference and (ii) the smallest thrombus area, in contrast to the largest thrombus area observed in Group 4 [SL(+) w/bump Wing], indicating excessive thrombosis (Fig. 4g). Marker gene expression of thrombotic features (vWF, PF-4, and P-sel) increases significantly from Group 2 to Group 3 and further to Group 4, except for vWF between Groups 2 and 3 (ns) (Fig. 4h).

As a phantom model of the thoracic aorta (Fig. S11), a silicone tube (ID: 8 mm, OD: 10 mm) was used, and 6 mm punctures were generated with a biopsy punch. The inner surface was coated with rat collagen type I by 1 h incubation, followed by spraying human vWF and reacting overnight to facilitate platelet adhesion. Test VWP groups were deployed into the punctures, which were then perfused with porcine whole blood at 750 mL min^{-1} for 5 min. Platelet adhesion increased

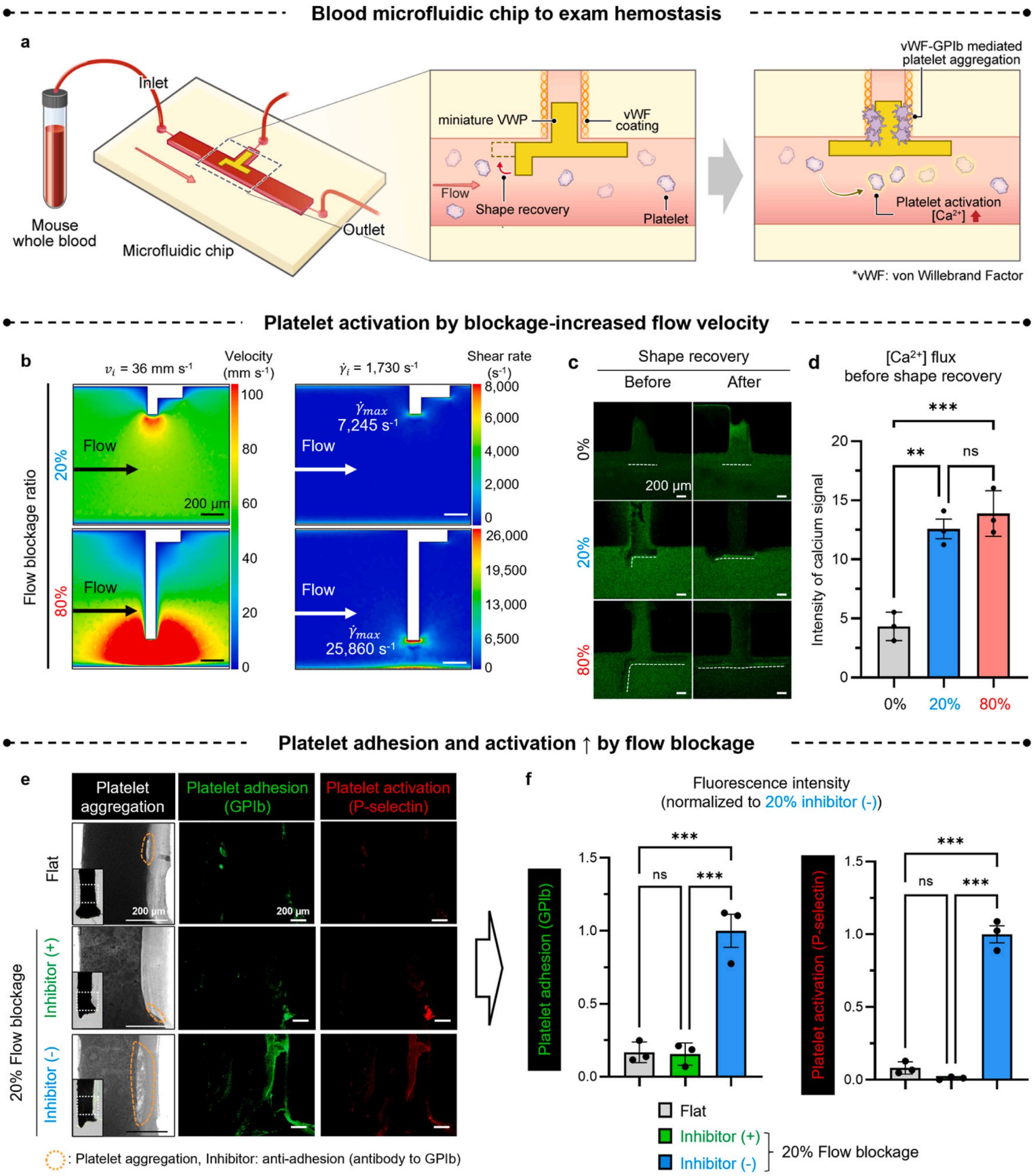

Fig. 3. Blood microfluidics with CFD to determine the Wing length by examining flow blockage and platelet responses. a, Mouse whole blood is perfused into a microfluidic chip as an in vitro model of vascular puncture. The curved Wing of the miniature VWP (mVWP) is coated with vWF to mediate platelet aggregation through vWF-GPIb signaling. The mVWP is deployed into the microfluidic channel so that blood platelets aggregate onto the Wing and become activated upon Ca^{2+} induction following shear gradients generated by partial flow blockage. **b,** In the CFD simulation, as the flow blockage ratio increases from 20 % to 80 %, the corresponding gradients in blood flow velocity (mm s^{-1}) and shear rate (s^{-1}) increases, indicating a regulatory role of Wing length in hemodynamics. **c,** After shape recovery of the Wing from 20 % to 80 % blockage ratios (curved), the lumen becomes cleared to the level of 0 % (flat) under confocal microscopy. **d,** The two blockage ratios result in no significant difference in intracellular calcium flux for platelet activation, while both maintain higher levels compared to 0 %. Thus the 20 % blockage ratio is selected for the follow-up experiments. **e,** The fluorescence images, together with **f,** the quantitative analysis, validate that the 20 % blockage by the curved Wing [inhibitor (−)] induces platelet adhesion (GPIb: green) and activation (P-selectin: red) significantly compared to the levels observed after shape recovery (flat). Inhibition of the vWF-GPIb interaction [inhibitor (+)] significantly reduces platelet responses to the levels of the flat condition, indicating a mechanistic role of vWF-GPIb interaction in mediating platelet responses under the 20 % flow blockage. Scale bars = 200 μm. Data are shown as mean ± SD, N = 3 biological replicates.

significantly from Group 2 to Group 3 and further to Group 4, indicating that Group 3 maintains a mild thrombotic level appropriate for hemostatic sealing. To mimic clinical cases, porcine carotid arteries were punctured (8 Fr; 2.67 mm) and deployed with commercial VCDs (suture-based, membrane-based, and PEG-based) or VWP for comparison (Fig. S12). The arteries were placed in a customized reactor and perfused with whole porcine blood at 750 mL min^{-1} for 5 min. Under FE-SEM, PEG-based samples exhibited significantly higher platelet adhesion than the others, while no significant differences were observed among VWP, suture-based, and membrane-based devices. This highlights the unique function of the VWP Wing, which uses a temporary increase in shear stress to promote hemostatic sealing without inducing materialdriven coagulation. Consequently, further thrombosis is suppressed once Ring recovery restores laminar blood flow.

3.5. Suturing-equivalent efficiency of VWP on 30-day closure of porcine aortic puncture

Suturing is considered the user-controlled standard for tightly closing vascular wall punctures [36,37]. Therefore, VWP and suturing were compared in their closure efficiency by generating two adjacent wall punctures (18 Fr; 6 mm) in the same thoracic aorta of each pig (Fig. 5a). Time to hemostasis was assessed on day 0, followed by evaluation of patency (angiography), wall stenosis (histology), re-endothelialization, and inflammation (IHC) on day 30. These timepoints were selected because bleeding and pseudoaneurysm occur immediately after closure, while stenosis, vascular injury, and ischemia are typically observed within one month. The final 30-day endpoint aligns with previous reports showing that endothelial coverage and wall maturation are largely complete within one month. In addition, ASTM F2477 requires 3.8 ×

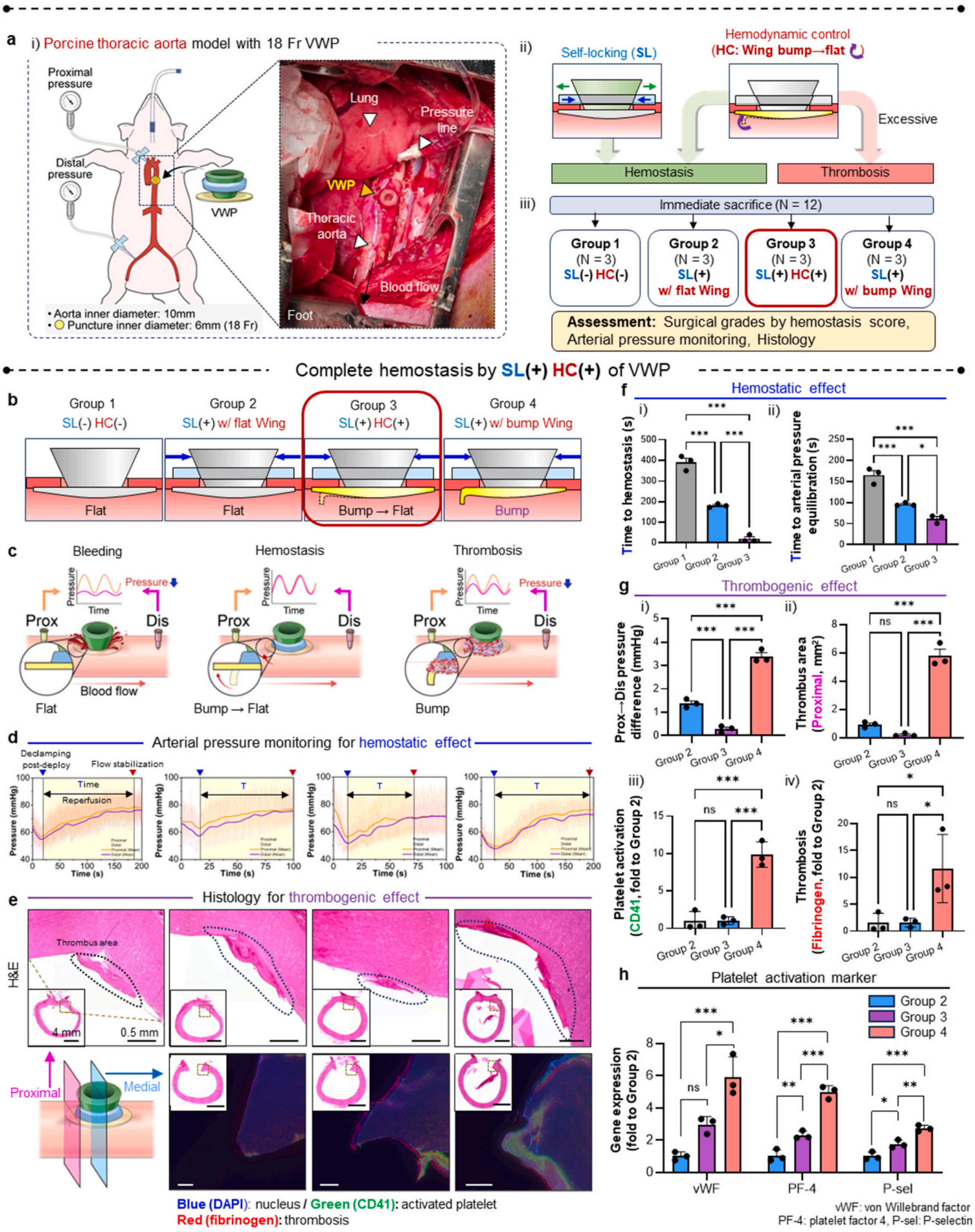

(caption on next page)

Fig. 4. 18 Fr puncture of hemostasis in porcine aorta using VWP by validating the memory programming effect of each part. a, As a challenging model for application of large-diameter catheters, i) an 18 Fr (6 mm) puncture is created into the porcine thoracic aorta (diameter: 10 mm) so that the size-matched VWP is deployed, followed by measuring proximal and distal blood pressure. ii) The experimental groups are designed first to exam the memory programming effect of collaboration between Ring squeezing with Body expansion on self-locking (SL) to enable efficient hemostasis. Next, the effect of Wing shape recovery from curve to flat is examined on hemodynamic control (HC) in cooperation with the actions of Body and Ring to handle hemostasis. No recovery of Wing shape is expected to induce excessive thrombosis. iii) Four experimental groups are established using a total of 12 pigs ($N = 12$) with immediate sacrifice following deployment ($N = 3$ each). Group 1 [SL(−) HC(−)] represents no memory programming. Group 2 [SL(+) w/flat Wing] has the effects of Body and Ring actions except the hemostatic sealing by keeping the flat Wing. Group 3 [SL(+) HC(+)] possesses the complete memory effects of the three parts. Group 4 [SL(+) w/bump Wing] is expected to have excessive thrombosis because of no shape recovery from the curved Wing while maintaining the memory actions of Body and Wing. **b,** Each group is visually explained in the illustrations. **c,** In VWP actions, (left) the bleeding condition preserves the normal sinusoidal waveform of high proximal pressure (green) in contrast to the disturbed waveform of low distal pressure (red). (middle) Hemostatic closure results in similar high sinusoidal waveform at both pressure sites. (right) Excessive thrombosis does not disturb the waveform, but the distal pressure level becomes lower than the proximal one. **d,** When reperfusion starts by removing the clamp post-deployment (blue), only Group 3 [SL(+) HC(+)] reaches the hemostatic closure, as evidenced by flow stabilization (red) with a 5 s plateau at both pressure sites. Group 4 [SL(+) w/bump Wing] exhibits the pattern of over-thrombosis. **e,** H&E images show bleeding in Group 1 as an indication of incomplete closure in contrast to moderate, minimal, and dense thrombotic features observed in Group 2, 3, and 4 respectively as further supported by the signals of activated platelets (green, CD41-positive) and fibrinogen (red) [Scale bars = 0.5 mm (4 mm in box)]. **f,** Compared to Group 1 [SL(−) HC(−)] and 2 [SL(+) w/flat Wing], Group 3 [SL(+) HC(+)] shows the fastest i) hemostasis and ii) arterial pressure equilibration, indicating the most efficient hemostatic response. **g,** These outcomes in Group 3 include i) the smallest difference between the proximal and distal pressures with ii) the smallest thrombus area in contrast the largest area of Group 4 [SL(+) w/bump Wing] as an indication of excessive thrombosis. **h,** The marker gene expression of thrombotic feature (vWF, PF-4, and P-sel) significantly increases from Group 2 to Group 3 and further to Group 4 except the comparison of vWF expression between Group 2 and 3 (ns: no significance). Data are shown as mean ± SD, $N = 3$ biologically independent animals per group. Significance was determined using one-way ANOVA with Tukey's test between groups.

10^8 cyclic strain loadings (20–60 Hz) to justify 10 years of stent use. SMP/PCL(95/5) maintains modulus and oscillation strain during 6×10^6 fatigue cycles at 0.1 MPa and 60 Hz (Fig. S3a), indicating >30-day durability under cyclic arterial loading. The closure status of both suture and VWP sites was confirmed photographically (Fig. 5b).

Continuous monitoring of proximal and distal arterial pressures showed the expected transitions: bleeding resulted in high proximal and low distal pressures, while hemostatic closure produced similar levels at both sites. After reperfusion was initiated by removing the vascular clamp (Fig. S14), both suture and VWP achieved hemostatic closure within the 65 s monitoring window, as defined by a stabilized 5 s pressure plateau. When hemostasis time on day 0 was assessed by i) visual scoring and ii) time to arterial pressure equilibration, VWP showed suturing-equivalent performance (Fig. 5c). On day 30, angiography demonstrated that VWP maintained i) vessel patency and ii) aortic diameter without stenosis, with no significant differences compared to suturing (Fig. 5d).

Upon harvesting the aorta (Fig. 5e), both closure sites exhibited no significant stenotic remodeling on H&E staining. This was supported by normal collagen and elastin features on Verhoeff–Van Gieson (VVG) staining and comparable re-endothelialization on CD31 immunostaining, with no differences in neointimal area. The adventitia in both groups showed microvessel (vasa vasorum) formation, indicated by sporadic CD31-positive spots. VWP induced regenerative M2 macrophage polarization with ARG-1 expression, accompanied by significantly greater macrophage (CD68-positive) infiltration into the adventitia compared to suturing. Marker gene expression in aortic adventitia was compared for Suture, VWP, and No-treat (intact wall) groups (Fig. S15). Both Suture and VWP exhibited significantly greater macrophage recruitment than No-treat, as indicated by CD68 and MCP1 expression. Furthermore, VWP promoted M2 polarization (ARG-1, IL-10), supporting adventitial regeneration, whereas TGFβ expression did not differ significantly among groups. This regenerative potential was also supported by higher EPC marker expression (CD31) in VWP compared to Suture and No-treat, while endothelial cell CD31 levels did not differ significantly among groups. Overall, VWP supports vascular wall regeneration from intima to adventitia despite bulky tissue formation, consistent with our previous study [38].

4. Discussion

Automation is an essential goal for reducing operator-dependent variability and ensuring the implantation safety of medical devices [39,40]. In line with trends in surgical robotics, preventing complications caused by erroneous or insufficiently trained skills is critical for maximizing clinical benefit [41,42]. Remote control through wireless triggers such as simple heating further strengthens automation because the user can choose the initiation timepoint while the remaining steps proceed automatically without requiring additional skill or vigilance [43–48]. This principle is central to the present study. VWP is designed to operate through a simple warm-water trigger once wall positioning is adjusted, which enables automated closure without technical demand. The underlying strategy is material programming, in which each component performs a pre-programmed action through shape memory. The SMP-based VWP coordinates SL and HC to close a large 6 mm thoracic aortic puncture under the highest physiological pressures of the circulatory system. This addresses a clear clinical unmet need. The tight sealing achieved by the memory-programmable VWP suggests that its pressure resistance is sufficient for catheterization scenarios regardless of puncture size or blood pressure.

Triggering VWP recovery at 45°C within 15 s is clinically safe because tissue injury begins only after more than 30 min of exposure to 45°C as reported previously [35]. Consistently, no tissue damage was observed in either animal study (Figs. 4 and 5), which supports that this level of heating is comparable to brief exposure to warm water (40–45°C). With a flow rate of 2.0 mL s^{-1}, the heat dissipates into blood and surrounding tissue, which physiologically maintains temperatures at or below approximately 43°C through homeostatic protection. Another critical design point is the orientation of the curved Wing. It must be deployed toward the proximal side of the puncture and aligned with flow direction to recruit and activate platelets under a transient increase in shear stress for hemostatic sealing. Mis-orientation would hinder the control of platelet activation and could lead to unintended thrombotic events.

The puncture size of abundant clinical cases is 6–7 Fr (≈2–2.3 mm) for deployment of stents and endovascular coronary imaging. In this study, the 18 Fr (≈6 mm) puncture of porcine aortic model is approached to validate the device function under large-bore puncture and the highest blood pressure. This model is to mimic a deployment model of transcatheter aortic valve replacement (TAVR), endovascular aneurysm repair (EVAR) or mechanical circulatory support (venoarterial-extracorporeal membrane oxygenation, VA-ECMO, and Impella) as mechanical auxiliary techniques. In addition to this in vivo model of large puncture, the ex vivo model of porcine carotid artery with 9 Fr (3 mm) is used to confirm the function of VWP under over 750 mmHg which is 10 times higher than the physiological range of porcine arterial pressure. Of note, open surgery was inevitable for imaging and filming during deployment of VWP into porcine aorta. The application system of VWP for delivery to fit in percutaneous means in a range of puncture size [6–7 Fr (≈2–2.3 mm) for stenting, angiography, and 18 Fr (≈6 mm) to

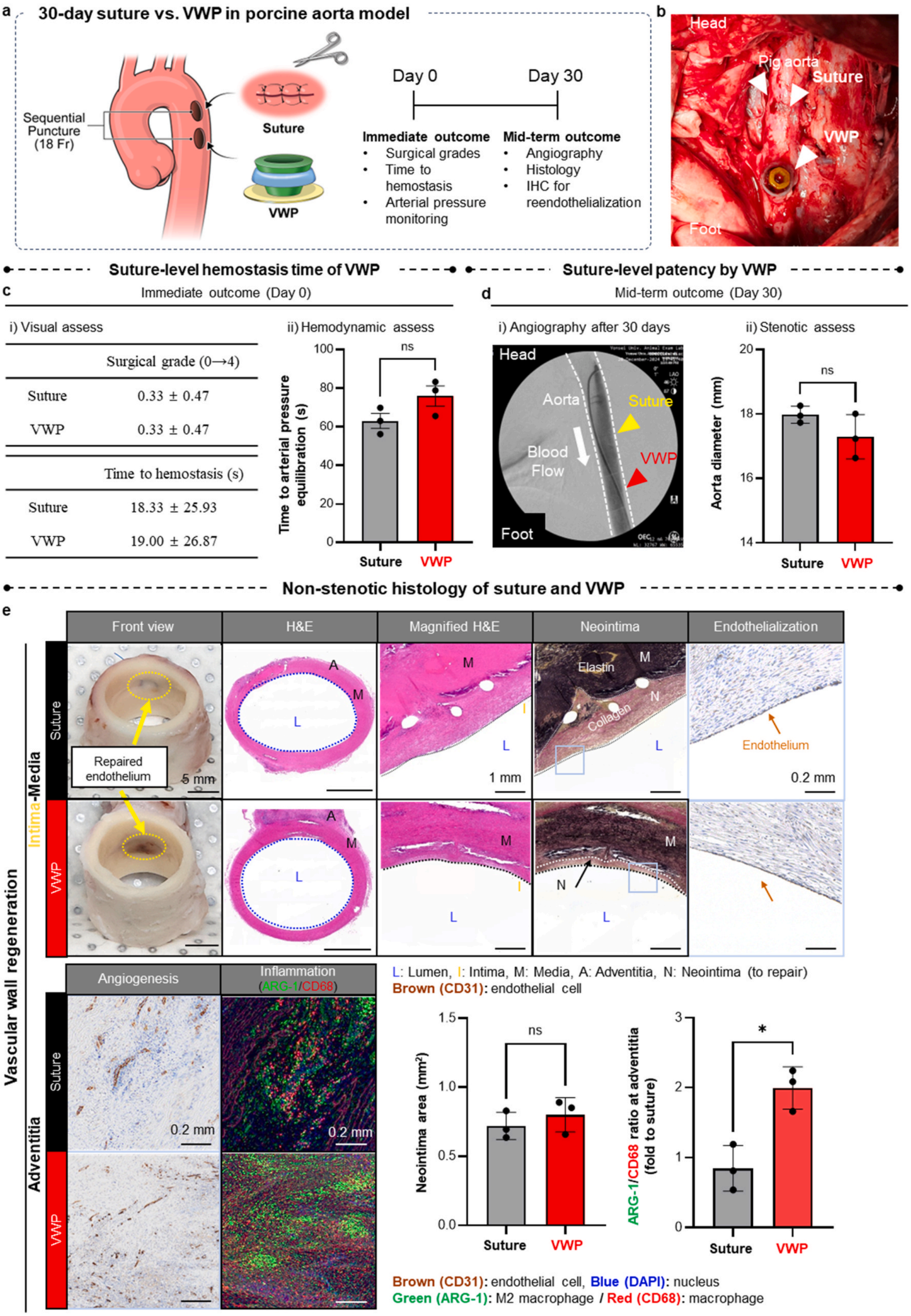

(caption on next page)

Fig. 5. Suturing-equivalent efficiency of VWP on 30 days puncture closure in porcine aortic wall. a, a, Suturing is considered as a user-controlled means to close vascular wall punctures. Hence, VWP is compared with suturing by creating two wall punctures (18 Fr: 6 mm) next to each other in the same thoracic aorta of each pig as illustrated. After assessing hemostasis time on day 0, the patency (angiography), wall stenosis (histology), and reendothelialization (IHC) are evaluated on day 30, since bleeding and pseudoaneurysm occur immediately, while stenosis, vascular injury and ischemia are clinically observed within one month post closure. **b,** The status of suturing and VWP deployment is photographically confirmed upon closing the sequential punctures in the porcine aortic wall. **c**, When hemostasis time is assessed on day 0 using i) visual scoring and ii) determining the time to arterial pressure equilibration, VWP demonstrates the suturing-equivalent results. **d,** On day 30, angiography shows that VWP manages i) the patency of blood flow and ii) the aortic diameter as non-stenotic indications, which are not significantly different from those of suturing. **e**, The two closure sites of suture and VWP are visualized in the photos after harvesting the aorta on day 30. Both groups exhibit no significant indications of stenotic wall remodeling in the hematoxylin and eosin (H&E) images. This is further supported by normal collagen and elastin features in Verhoeff–Van Gieson (VVG) staining in addition to re-endothelialization by CD31 immunohistochemistry with no significant difference in the neointimal area. Likewise, the adventitia of both samples exhibits the features of microvessel (vasa vasorum) formation as indicated by sporadic CD31-positive spots. In association, VWP induces regenerative M2 polarization with ARG-1 expression upon significantly more invasion of macrophages (CD68-positive) into adventitia compared to Suture. Hence, VWP supports regeneration of vascular wall from intima to adventitia despite bulky tissue formation. [Scale bars = 5 mm (gross and H&E), 1 mm (Magnified H&E and VVG stain) and 0.2 mm (CD31)]. Data are shown as mean ± SD, N = 3 biological replicates.

TAVR, EVAR, VA-ECMO, Impella] should be approached in the future. Although the puncture size is somewhat larger or smaller during deployment into the body, no clear issue is foreseen because Ring squeezing is to pull the surrounding wall tissue while Body expansion and Wing hemostasis are to tighten puncture closing and sealing.

Another impactful point of this study is that the dynamic nature of blood responses is used as a sealing mechanism, followed by recovery of healthy pressure and flow characteristics. Heparin circulating during VWP implantation in pigs does not hinder the plugging function, and no thrombotic issues were observed in histological or angiographic analyses. After platelets encounter the curved Wing under blood flow, the increased shear rate induces platelet aggregation and activation, enabling hemostatic sealing with leakage-free closure of the puncture. The shape recovery of the Wing prevents further thrombosis by preserving laminar blood flow, which eliminates the risk of vessel occlusion and cooperates with the mitigation of platelet adhesion by SMP/PCL. This mechanism represents a unique mode of action by which VWP manages both sealing and thrombosis.

Current VCDs, including Suture-based (Perclose Proglide, Abbott), Membrane-based (Femoseal, Terumo), and PEG-based (Mynx Control, Cordis), are effective in closing punctures ≤7 Fr but are limited in >18 Fr punctures. The present results indicate promising potential for VWP to address this range of large punctures. Because existing VCDs depend primarily on thrombosis for sealing through intravascular plugging, suturing, or absorption, patients who are under anti-coagulation therapies after stenting can face risks of incomplete hemostasis and rebleeding. Hemodynamic control by VWP, combined with mitigation of excessive thrombosis, offers an advantage in this context, as supported by successful outcomes in the porcine aortic model with circulating anticoagulative heparin. Moreover, current VCDs require skill-dependent operation from positioning to deployment. In comparison, VWP operation can be completed by injecting warm saline within 15 s once positioning is finalized before heating.

The timer-based switching from thrombotic induction to a restorative stage provides a driving force for endothelialization by suppressing pathological vascular wall remodeling. This mechanism resembles the behavior seen in suturing-based tissue adhesion, where tight integration among damaged tissues establishes conditions necessary for wound healing [49]. Filling the gap with beneficial reactions by inflammatory cells (M2 polarization) creates a foundation for neighboring ECs to migrate and form a lining with tight junctions (endothelium) on the flattened Wing as the thrombus resolves [50]. When blood flow interacts with the curved Wing, endothelial progenitor cells (EPCs) from circulation may also land at the deployment site [51]. ECs regulate the responses of vascular smooth muscle cells and fibroblasts within the vascular wall, as well as inflammatory cells, through cytokines, nitric oxide, and growth factors [52,53]. Reendothelialization is therefore a critical consideration for implantable vascular devices, such as endovascular stents, artificial blood vessels, and vascular anastomotic couplers [54,55]. Self-locking allows vascular wall tissues to be tightly secured within the puncture space, and hemodynamic control facilitates rapid primary hemostasis as flow interacts with the Wing, promoting platelet recruitment and potentially EPC deposition. These events initiate the healing process while suppressing pathological changes. Moreover, hemodynamic control is made possible through CFD simulation with experimental validation in whole blood microfluidics. Gradients of shear stress and velocity are calculated through CFD using a model of incremental intramural thrombus, and the results are applied to determine the optimized flow blockage ratio. This process provides substantial advantages in strategizing platelet activation by the curved Wing, and variation of the blockage ratio can be evaluated using the blood microfluidic model of VWP deployment. This convergent approach, from computation to a miniature experimental model, minimizes trial and error in programming the Wing shape recovery before applying it to the porcine aortic model.

When the multi-level technologies are examined at higher resolution, SMP plays a central role in controlling VWP functions. SMPs are also tuned to facilitate the deployment process by adjusting the degree of ring strain and blending with phase behavior. The toughness of SMP to resist burst pressure increases as homogeneous blending reduces unstable phase boundaries while maintaining high crystallinity. Results from in vitro, ex vivo, and in vivo experiments, supported by computational analyses, validate that VWP function is reliable across different vessel sizes, physiological pressures, and blood volumes. These findings indicate clinical potential to provide consistent outcomes across patients under various pathophysiological conditions. Hence, this study presents an unprecedented model merging multidisciplinary techniques with multi-level validations. The translatable solution is proposed as a memory-programmable VWP that addresses unmet needs in current VCD applications.

Regarding clinical advantages, VWP deployment is minimally invasive, as standard sheaths and catheters used in current percutaneous procedures are compatible. Compatibility with commercial sheaths and catheters has been confirmed, and percutaneous access to large aortic punctures under high blood pressure is feasible. Additionally, the use of pushers and thread allows repositioning of VWP insertion when initial placement is insufficiently accurate. VWP enables rapid hemostasis similar to surgical suturing and does not induce pathogenic vascular remodeling, as supported by the presence of normal endothelium and wall structure with suppression of neointima and fibrosis, indicating regenerative potential. M2 polarization of macrophages, combined with increased EPC signature in the adventitia, further enhances this regenerative potential by rescuing ischemic tissue through the formation of vasa vasorum-like microvessels. These foundational results position VWP for the next steps toward clinical translation, especially when compared with commercial VCDs such as suturing, clipping, and absorbent plugging types.

Despite the advantages of the present study, several important subjects remain for future investigation. First, VWP biodegradation over time may support regeneration of the vascular wall in cases where permanent implantation is considered. We have recently developed biodegradable SMP for bone regeneration [22]. Applying biodegradability to VWP will require careful study of degradation rate to support vascular wall regeneration without premature loss of mechanical properties necessary to resist burst pressure. Second, re-use of the puncture site for repeated catheter deployment should be explored through development of a two-way shape memory system. In this system, VWP would transition from a deployable structure to a plugging structure upon swelling, followed by a return to the deployable structure upon heating, allowing easy removal for re-use of the puncture. A new class of SMPs is currently under development that uses swelling as the first trigger for shape recovery from the temporary to the original structure, and heating as the second trigger to revert from the original structure to the temporary one. Third, following the trend of laparoscopy, a device enabling minimally invasive deployment of VWP should be considered. This approach should further reduce skill dependency and minimize incision size by improving the accuracy of puncture targeting. Finally, when device manufacturing is scaled, quality reproducibility must be ensured, starting with PDMS mold-based casting, which offers advantages in controlling structural accuracy and consistent shape programming. This approach must be advanced to support scalable micro-molding under good manufacturing practice (GMP) conditions for clinical translation.

CRediT authorship contribution statement

Sungwoo Cho: Writing – original draft, Visualization, Validation, Supervision, Software, Project administration, Methodology, Investigation, Formal analysis, Data curation, Conceptualization. **Hyun-Su Ha:** Writing – original draft, Visualization, Validation, Methodology, Investigation, Formal analysis, Data curation. **Sangmin Lee:** Visualization, Validation, Methodology, Investigation, Formal analysis, Data curation. **Hyunjae Kim:** Methodology, Investigation, Data curation. **Seok Joon Lee:** Methodology, Investigation. **Jueun Kim:** Methodology, Investigation. **Yerin Lee:** Methodology, Investigation. **Kang Suk Lee:** Methodology, Investigation. **Hyun-Chel Joo:** Validation, Supervision, Resources, Project administration, Methodology, Investigation. **Hak-Joon Sung:** Writing – original draft, Supervision, Resources, Project administration, Funding acquisition, Conceptualization.

Ethics approval and consent to participate statements

All animal experiments were carried out in accordance with the Institutional Animal Care and Use Committee of Yonsei University College of Medicine (IACUC, approval number: 2024-0296, 2022-0050).

Declaration of competing interest

The authors declare that they have no known competing financial interests or personal relationships that could have appeared to influence the work reported in this paper.

Acknowledgment

S. Cho., H. Ha., and S. Lee contributed equally to this work as co-first authors. H.-J.S. is listed as the lead corresponding author in addition to H.C.J. This research was supported by Basic Science Research Program through the National Research Foundation of Korea (NRF) funded by the Ministry of Science and ICT (RS-2023-00302125) in addition to a grant of the Korea Health Technology R&D Project through the Korea Health Industry Development Institute (KHIDI) funded by the Ministry of Health & Welfare, Republic of Korea (RS-2023-00265566).

Appendix A. Supplementary data

Supplementary data to this article can be found online at https://doi.org/10.1016/j.bioactmat.2025.12.042.

References

[1] L. Paraggio, F. Bianchini, C. Aurigemma, E. Romagnoli, E. Bianchini, A. Zito, M. Lunardi, C. Trani, F. Burzotta, Femoral large bore sheath management: how to prevent vascular complications from vessel puncture to sheath removal, Circulation: Cardiovascular Interventions 17 (2024) e014156, https://doi.org/10.1161/CIRCINTERVENTIONS.124.014156.

[2] S.V. Rao, G.W. Stone, Arterial access and arteriotomy site closure devices, Nat. Rev. Cardiol. 13 (2016) 641–650, https://doi.org/10.1038/nrcardio.2016.133.

[3] A.J. Chase, E.B. Fretz, W.P. Warburton, W.P. Klinke, R.G. Carere, D. Pi, B. Berry, J. D. Hilton, Association of the arterial access site at angioplasty with transfusion and mortality: the MORTAL study (Mortality benefit of reduced transfusion after percutaneous coronary intervention via the arm or leg), Heart 94 (2008) 1019–1025, https://doi.org/10.1136/hrt.2007.136390.

[4] N. Pang, J. Gao, B. Zhang, M. Guo, N. Zhang, M. Sun, R. Wang, Vascular closure devices versus manual compression in cardiac interventional procedures: systematic review and meta-analysis, cardiovascular therapeutics 2022. https://doi.org/10.1155/2022/8569188, 2022.

[5] M. Tavakol, S. Ashraf, S.J. Brener, Risks and complications of coronary angiography: a comprehensive review, Global J. Health Sci. 4 (2012) 65, https://doi.org/10.5539/gjhs.v4n1p65.

[6] L.-Q. Hon, A. Ganeshan, S.M. Thomas, D. Warakaulle, J. Jagdish, R. Uberoi, Vascular closure devices: a comparative overview, Current problems in diagnostic radiology 38 (2009) 33–43, https://doi.org/10.1067/j.cpradiol.2008.02.002.

[7] S. Schulz-Schüpke, S. Helde, S. Gewalt, T. Ibrahim, M. Linhardt, K. Haas, K. Hoppe, C. Böttiger, P. Groha, C. Bradaric, Comparison of vascular closure devices vs manual compression after femoral artery puncture: the ISAR-CLOSURE randomized clinical trial, JAMA 312 (2014) 1981–1987, https://doi.org/10.1001/jama.2014.15305.

[8] V.J. Noori, J. Eldrup-Jørgensen, A systematic review of vascular closure devices for femoral artery puncture sites, J. Vasc. Surg. 68 (2018) 887–899, https://doi.org/10.1016/j.jvs.2018.05.019.

[9] K. Sarathy, K.P. Patel, D.M. Jones, M. Akhtar, V. Khanna, C. Broyd, M. Ozkor, S. Kennon, A. Mathur, A. Baumbach, Large bore vascular access closure device strategies, Structural Heart 5 (2021) 186–191, https://doi.org/10.1080/24748706.2021.1872818.

[10] H.L. Dauerman, R.J. Applegate, D.J. Cohen, Vascular closure devices: the second decade, J. Am. Coll. Cardiol. 50 (2007) 1617–1626, https://doi.org/10.1016/j.jacc.2007.07.028.

[11] M.P. van Wiechen, J.M. Ligthart, N.M. Van Mieghem, Large-bore vascular closure: new devices and techniques, Intervent Cardiol. 14 (2019) 17, https://doi.org/10.15420/icr.2018.36.1.

[12] V.D. Vidi, M.E. Matheny, U.S. Govindarajulu, S.-L.T. Normand, S.L. Robbins, V. V. Agarwal, S. Bangalore, F.S. Resnic, Vascular closure device failure in contemporary practice, JACC Cardiovasc. Interv. 5 (2012) 837–844, https://doi.org/10.1016/j.jcin.2012.05.005.

[13] S. Bangalore, N. Arora, F.S. Resnic, Vascular closure device failure: frequency and implications: a propensity-matched analysis, Circulation: Cardiovascular Interventions 2 (2009) 549–556, https://doi.org/10.1161/CIRCINTERVENTIONS.109.877407.

[14] A.M. Ierardi, A. Coppola, M. Renzulli, F. Piacentino, F. Fontana, A. Paladini, G. Guzzardi, V. Semeraro, C. Di Stasi, F. Giurazza, Effectiveness and safety of different vascular closure devices: Multicentre prospective observational study, Cardiovascular and interventional radiology 46 (2023) 827–834, https://doi.org/10.1007/s00270-023-03513-y.

[15] F.S. Resnic, T.Y. Wang, N. Arora, V. Vidi, D. Dai, F.-S. Ou, M.E. Matheny, Quantifying the learning curve in the use of a novel vascular closure device: an analysis of the NCDR (National Cardiovascular Data Registry) CathPCI registry, JACC Cardiovasc. Interv. 5 (2012) 82–89, https://doi.org/10.1016/j.jcin.2011.09.017.

[16] I.-M. Chen, T.-H. Lee, P.-L. Chen, C.-C. Shih, H.-H. Chang, Factors in ProGlide® vascular closure failure in sheath arteriotomies greater than 16 French, Eur. J. Vasc. Endovasc. Surg. 58 (2019) 615–622, https://doi.org/10.1016/j.ejvs.2019.03.037.

[17] N.M. Van Mieghem, A. Latib, J. Van Der Heyden, L. Van Gils, J. Daemen, T. Sorzano, J. Ligthart, K. Witberg, T. De Kroon, N. Maor, Percutaneous plug-based arteriotomy closure device for large-bore access: a multicenter prospective study, JACC Cardiovasc. Interv. 10 (2017) 613–619, https://doi.org/10.1016/j.jcin.2016.12.277.

[18] M.A. Gimbrone Jr., G. García-Cardeña, Endothelial cell dysfunction and the pathobiology of atherosclerosis, Circ. Res. 118 (2016) 620–636, https://doi.org/10.1161/CIRCRESAHA.115.306301.

[19] Y.C. Shin, J.B. Lee, D.H. Kim, T. Kim, G. Alexander, Y.M. Shin, J.Y. Park, S. Baek, J. K. Yoon, Y.J. Lee, Development of a shape-memory tube to prevent vascular stenosis, Adv. Mater. 31 (2019) 1904476, https://doi.org/10.1002/adma.201904476.

[20] S.W. Yi, Y.M. Shin, J.B. Lee, J.Y. Park, D.H. Kim, W. Baek, J.K. Yoon, D.G. Kim, I. S. Shin, C.S. Kim, Dilation-responsive microshape programing prevents vascular graft stenosis, Small 17 (2021) 2007297, https://doi.org/10.1002/smll.202007297.

[21] Y. Hong, I. Azcune, A. Rekondo, T. Jiang, S. Zhou, T. Lowe, E. Saiz, Additive manufacturing of shape memory thermoset composites with directional thermal conductivity, Adv. Funct. Mater. 34 (2024) 2311193.

[22] S. Cho, K.S. Lee, K. Lee, H.S. Kim, S. Park, S.E. Yu, H. Ha, S. Baek, J. Kim, H. Kim, Surface crystal and degradability of shape memory scaffold essentialize

osteochondral regeneration, Small 20 (2024) 2401989, https://doi.org/10.1002/smll.202401989.

[23] H. Ha, C.H. Lee, K.S. Lee, K. Lee, J. Park, S.Y. Kim, S. Baek, M.L. Kang, D.W. Lee, H. J. Sung, Shape-configurable mesh for hernia repair by synchronizing anisotropic body motion, Small 19 (2023) 2303325, https://doi.org/10.1002/smll.202303325.

[24] H. Ha, J.Y. Park, C.H. Lee, D.H. Son, S.W. Chung, S. Baek, K. Lee, K.S. Lee, S.W. Yi, M.L. Kang, Vascular cast to program antistenotic hemodynamics and remodeling of vein graft, Adv. Sci. 10 (2023) 2204993, https://doi.org/10.1002/advs.202204993.

[25] W. Zhao, Z. Huang, L. Liu, W. Wang, J. Leng, Y. Liu, Porous bone tissue scaffold concept based on shape memory PLA/Fe3O4, Compos. Sci. Technol. 203 (2021) 108563.

[26] L. Nash, C. Yeh, A. Holden, M. Reijnen, D. Maitland, Shape memory polymer embolization scaffolds for treating abdominal aortic aneurysms. Shape Memory Polymer Embolization Scaffolds for Treating Abdominal Aortic Aneurysms, MARY ANN LIEBERT, INC 140 HUGUENOT STREET, 3RD FL, NEW ROCHELLE, NY 10801 USA, 2024, pp. S161–S162.

[27] M.A. Yousefi, D. Rahmatabadi, M. Baniassadi, M. Bodaghi, M. Baghani, 4D printing of multifunctional and biodegradable PLA-PBAT-Fe3O4 nanocomposites with supreme mechanical and shape memory properties, Macromol. Rapid Commun. 46 (2025) 2400661.

[28] O. Oshinowo, S.S. Azer, J. Lin, W.A. Lam, Why platelet mechanotransduction matters for hemostasis and thrombosis, J. Thromb. Haemostasis 21 (2023) 2339–2353, https://doi.org/10.1016/j.jtha.2023.06.010.

[29] R. Kaiser, R. Escaig, L. Nicolai, Hemostasis without clot formation: how platelets guard the vasculature in inflammation, infection, and malignancy, Blood 142 (2023) 1413–1425, https://doi.org/10.1182/blood.2023020535.

[30] Y. Chen, L.A. Ju, F. Zhou, J. Liao, L. Xue, Q.P. Su, D. Jin, Y. Yuan, H. Lu, S. P. Jackson, An integrin αIIbβ3 intermediate affinity state mediates biomechanical platelet aggregation, Nat. Mater. 18 (2019) 760–769, https://doi.org/10.1038/s41563-019-0323-6.

[31] L.H. Ting, S. Feghhi, N. Taparia, A.O. Smith, A. Karchin, E. Lim, A.S. John, X. Wang, T. Rue, N.J. White, Contractile forces in platelet aggregates under microfluidic shear gradients reflect platelet inhibition and bleeding risk, Nat. Commun. 10 (2019) 1204, https://doi.org/10.1038/s41467-019-09150-9.

[32] W.S. Nesbitt, E. Westein, F.J. Tovar-Lopez, E. Tolouei, A. Mitchell, J. Fu, J. Carberry, A. Fouras, S.P. Jackson, A shear gradient–dependent platelet aggregation mechanism drives thrombus formation, Nature medicine 15 (2009) 665–673, https://doi.org/10.1038/nm.1955.

[33] Y. Hou, N. Carrim, Y. Wang, R.C. Gallant, A. Marshall, H. Ni, Platelets in hemostasis and thrombosis: novel mechanisms of fibrinogen-independent platelet aggregation and fibronectin-mediated protein wave of hemostasis, Journal of biomedical research 29 (2015) 437, https://doi.org/10.7555/JBR.29.20150121.

[34] C.H.H. Chan, M. Inoue, K.K. Ki, T. Murashige, J.F. Fraser, M.J. Simmonds, G. D. Tansley, N. Watanabe, Shear-dependent platelet aggregation size, Artif. Organs 44 (2020) 1286–1295, https://doi.org/10.1111/aor.13783.

[35] A. Moritz, The relative importance of time and surface temperature in causation of cataneous burns, stadiesm of thermal injury, Am. J. Pathol. 23 (1947).

[36] M.P. van Wiechen, D. Tchétché, J.F. Ooms, T.W. Hokken, H. Kroon, F. Ziviello, A. Ghattas, S. Siddiqui, C. Laperche, E. Spitzer, Suture-or plug-based large-bore arteriotomy closure: a pilot randomized controlled trial, Cardiovascular Interventions 14 (2021) 149–157.

[37] G.B. Torsello, B. Kasprzak, E. Klenk, J. Tessarek, N. Osada, G.F. Torsello, Endovascular suture versus cutdown for endovascular aneurysm repair: a prospective randomized pilot study, J. Vasc. Surg. 38 (2003) 78–82.

[38] H.s. Ha, S. Baek, K. Lee, S. Cho, M.J. Cho, S. Chung, H. Choi, C.H. Lee, M.S. Kim, S. Y. Kim, Artificial vasa-vasorum serves as an on-site regenerative promoter of cell-free vascular grafting, Adv. Funct. Mater. 34 (2024) 2315310.

[39] L. Hon, A. Ganeshan, S. Thomas, D. Warakaulle, J. Jagdish, R. Uberoi, An overview of vascular closure devices: what every radiologist should know, European journal of radiology 73 (2010) 181–190.

[40] V.P. Krishnasamy, M.J. Hagar, D.J. Scher, M.L. Sanogo, G.E. Gabriel, S.N. Sarin, Vascular closure devices: technical tips, complications, and management, Tech. Vasc. Intervent. Radiol. 18 (2015) 100–112.

[41] J. Bonatti, G. Vetrovec, C. Riga, O. Wazni, P. Stadler, Robotic technology in cardiovascular medicine, Nat. Rev. Cardiol. 11 (2014) 266–275.

[42] G. Ciuti, R.J. Webster III, K.-W. Kwok, A. Menciassi, Robotic surgery, Nature Reviews Bioengineering (2025) 1–14.

[43] R. Takagi, K. Osada, A. Hanafusa, M. Takagi, S.B. Mohamaddan, K. Mitsui, H. Anzai, Development of a remote-control system for catheterization capable of high-speed force feedback, Int. J. Comput. Assist. Radiol. Surg. 18 (2023) 763–773.

[44] R.H. Soon, Z. Ren, W. Hu, U. Bozuyuk, E. Yildiz, M. Li, M. Sitti, On-demand anchoring of wireless soft miniature robots on soft surfaces, Proc. Natl. Acad. Sci. 119 (2022) e2207767119.

[45] W. Zhao, F. Zhang, J. Leng, Y. Liu, Personalized 4D printing of bioinspired tracheal scaffold concept based on magnetic stimulated shape memory composites, Compos. Sci. Technol. 184 (10) (2019), 1016.

[46] W. Zhao, C. Yue, L. Liu, Y. Liu, J. Leng, Research progress of shape memory polymer and 4D printing in biomedical application, Adv. Healthcare Mater. 12 (2023) 2201975.

[47] D. Rahmatabadi, M.A. Yousefi, S. Shamsolhodaei, M. Baniassadi, K. Abrinia, M. Bodaghi, M. Baghani, 4D printing of polyethylene glycol-grafted carbon nanotube-reinforced polyvinyl chloride–polycaprolactone composites for enhanced shape recovery and thermomechanical performance, Adv. Intell. Syst. (2025) 2500113.

[48] K. Mirasadi, M.A. Yousefi, L. Jin, D. Rahmatabadi, M. Baniassadi, W.H. Liao, M. Bodaghi, M. Baghani, 4D printing of magnetically responsive shape memory polymers: toward sustainable solutions in soft robotics, wearables, and biomedical devices, Adv. Sci. (2025) e13091.

[49] G.C. Gurtner, S. Werner, Y. Barrandon, M.T. Longaker, Wound repair and regeneration, Nature 453 (2008) 314–321.

[50] Y. Wallez, P. Huber, Endothelial adherens and tight junctions in vascular homeostasis, inflammation and angiogenesis, Biochimica et Biophysica Acta (BBA)-Biomembranes 1778 (2008) 794–809.

[51] A.G. Kutikhin, M.Y. Sinitsky, A.E. Yuzhalin, E.A. Velikanova, Shear stress: an essential driver of endothelial progenitor cells, Journal of Molecular and Cellular Cardiology 118 (2018) 46–69.

[52] C.E. Evans, M.L. Iruela-Arispe, Y.-Y. Zhao, Mechanisms of endothelial regeneration and vascular repair and their application to regenerative medicine, Am. J. Pathol. 191 (2021) 52–65.

[53] J. Amersfoort, G. Eelen, P. Carmeliet, Immunomodulation by endothelial cells—partnering up with the immune system? Nat. Rev. Immunol. 22 (2022) 576–588.

[54] S. Jana, Endothelialization of cardiovascular devices, Acta Biomater. 99 (2019) 53–71.

[55] D.G. Seifu, A. Purnama, K. Mequanint, D. Mantovani, Small-diameter vascular tissue engineering, Nat. Rev. Cardiol. 10 (2013) 410–421.